

HADES RV programme with HARPS-N at TNG^{★,★★}

XIV. A candidate super-Earth orbiting the M-dwarf GJ 9689 with a period close to half the stellar rotation period

J. Maldonado¹, A. Petralia¹, M. Damasso², M. Pinamonti², G. Scandariato³, E. González-Álvarez⁴, L. Affer¹, G. Micela¹, A. F. Lanza³, G. Leto³, E. Poretti^{5,6}, A. Sozzetti², M. Perger^{7,8}, P. Giacobbe², R. Zanmar Sánchez³, A. Maggio¹, J. I. González Hernández^{9,10}, R. Rebolo^{9,10}, I. Ribas^{7,8}, A. Suárez-Masareño^{9,10}, B. Toledo-Adroán^{9,10}, A. Bignamini¹¹, E. Molinari¹², E. Covino¹³, R. Claudi¹⁴, S. Desidera¹⁴, E. Herrero^{7,8}, J. C. Morales^{7,8}, I. Pagano³, and G. Piotto¹⁵

¹ INAF - Osservatorio Astronomico di Palermo, Piazza del Parlamento 1, 90134 Palermo, Italy
e-mail: jesus.maldonado@inaf.it

² INAF - Osservatorio Astrofisico di Torino, Via Osservatorio 20, 10025 Pino Torinese, Italy

³ INAF - Osservatorio Astrofisico di Catania, Via S. Sofia 78, 95123, Catania, Italy

⁴ Centro de Astrobiología (CSIC-INTA), Carretera de Ajalvir km 4, 28850 Torrejón de Ardoz, Madrid, Spain

⁵ Fundación Galileo Galilei-INAf, Rambla José Ana Fernández Pérez 7, 38712 Breña Baja, TF, Spain

⁶ INAF - Osservatorio Astronomico di Brera, Via E. Bianchi 46, 23807 Merate, Italy

⁷ Institut de Ciències de l'Espai (ICE, CSIC), Campus UAB, Carrer de Can Magrans s/n, 08193 Bellaterra, Spain

⁸ Institut d'Estudis Espacials de Catalunya (IEEC), 08034 Barcelona, Spain

⁹ Instituto de Astrofísica de Canarias, 38205 La Laguna, Tenerife, Spain

¹⁰ Universidad de La Laguna, Departamento Astrofísica, 38206 La Laguna, Tenerife, Spain

¹¹ INAF - Osservatorio Astronomico di Trieste, Via Tiepolo 11, 34143 Trieste, Italy

¹² INAF - Osservatorio Astronomico di Cagliari & REM, Via della Scienza, 5, 09047 Selargius CA, Italy

¹³ INAF - Osservatorio Astronomico di Capodimonte, Salita Moiriello 16, 80131 Napoli, Italy

¹⁴ INAF - Osservatorio Astronomico di Padova, vicolo dell'Osservatorio 5, 35122 Padova, Italy

¹⁵ Dipartimento di Fisica e Astronomia Galileo Galilei, Vicolo Osservatorio 3, 35122 Padova, Italy

Received ; accepted

ABSTRACT

Context. It is now well-established that small, rocky planets are common around low-mass stars. However, the detection of such planets is challenged by the short-term activity of the host stars.

Aims. The HARPS-N red Dwarf Exoplanet Survey (HADES) program is a long-term project at the Telescopio Nazionale Galileo aimed at the monitoring of nearby, early-type, M dwarfs, using the HARPS-N spectrograph to search for small, rocky planets.

Methods. A total of 174 HARPS-N spectroscopic observations of the M0.5V-type star GJ 9689 taken over the past seven years have been analysed. We combined these data with photometric measurements to disentangle signals related to the stellar activity of the star from possible Keplerian signals in the radial velocity data. We run an MCMC analysis, applying Gaussian Process regression techniques to model the signals present in the data.

Results. We identify two periodic signals in the radial velocity time series, with periods of 18.27 d, and 39.31 d. The analysis of the activity indexes, photometric data, and wavelength dependency of the signals reveals that the 39.31 d signal corresponds to the stellar rotation period. On the other hand, the 18.27 d signal shows no relation to any activity proxy or the first harmonic of the rotation period. We, therefore, identify it as a genuine Keplerian signal. The best-fit model describing the newly found planet, GJ 9689 b, corresponds to an orbital period $P_b = 18.27 \pm 0.01$ d, and a minimum mass $M_p \sin i = 9.65 \pm 1.41 M_\oplus$.

Key words. techniques: spectroscopic -stars: late-type -stars: planetary systems -stars: individual: GJ 9689

1. Introduction

Starting with the first exoplanet discoveries (Wolszczan & Frail 1992; Mayor & Queloz 1995) astronomers have succeeded in

unravelling an astonishing diversity of planetary systems, compositions, and host stellar properties (e.g. Udry & Santos 2007; Cumming 2010; Howard 2013; Perryman 2018).

Low-mass stars or M dwarfs constitute the most common stellar component in the Milky Way (e.g. Chabrier & Baraffe 2000). However, unlike their FGK counterparts, results regarding the properties of planets around M dwarfs still focus on small sample sizes and suffer from the intrinsic difficulties in the spectral characterisation of M dwarfs. In spite of their high levels of stellar variability and their intrinsic faintness at optical

[★] Based on observations made with the Italian *Telescopio Nazionale Galileo* (TNG) operated by the *Fundación Galileo Galilei* (FGG) of the *Istituto Nazionale di Astrofisica* (INAF) at the *Observatorio del Roque de los Muchachos* (La Palma, Canary Islands, Spain).

^{★★} Table A.1 is only available in electronic form at the CDS via anonymous ftp to [cdsarc.u-strasbg.fr](ftp://cdsarc.u-strasbg.fr) (130.79.128.5) or via <http://cdsweb.u-strasbg.fr/cgi-bin/qcat?J/A+A/>

wavelengths, it is now widely accepted that low-mass stars are optimal targets around which to search for small rocky planets (e.g. Dressing & Charbonneau 2013, 2015) and a large number of both radial velocity as the HET and HPF M dwarf surveys (Endl et al. 2003; Wright et al. 2018), the HARPS-GTO programme (Bonfils et al. 2013), the HADES survey (Affer et al. 2016), CARMENES (e.g. Zechmeister et al. 2019), SPIRou (e.g. Klein et al. 2021), or SOPHIE (e.g. Hobson et al. 2019), and photometric surveys like MEarth (Nutzman & Charbonneau 2008), APACHE (Sozzetti et al. 2013), TRAPPIST (Gillon, M. et al. 2012), or TESS (e.g. Feliz et al. 2021) are currently focused on M dwarfs.

At the time of writing there are ~ 130 known radial velocity planets around M dwarfs listed in The Extrasolar Planets Encyclopaedia (Schneider et al. 2011)¹, and several interesting trends regarding the properties of planets around M dwarfs have already been discussed. It has been established that, unlike their solar-type counterparts, the frequency of gas-giant planets orbiting low-mass stars is low (Endl et al. 2003, 2006; Butler et al. 2006; Bonfils et al. 2007; Cumming et al. 2008; Johnson et al. 2010). On the other hand, as found for FGK stars, small planets orbiting M dwarfs seem to be very abundant, most of them in multi planet systems. The HARPS-M dwarf survey reports a 36% occurrence for super-Earths ($M_p \sin i < 10 M_\oplus$) in short periods ($P < 10$ d) and 52% for $10 \text{ days} < P < 100$ d (Bonfils et al. 2013). Tuomi et al. (2014) estimates a frequency of low-mass planets around M dwarfs of one planet per star, possibly even greater. Results from the KEPLER mission suggest that the frequency of planets (with periods below 50 days) around stars seems to increase as we move from F stars towards the M dwarf type (Howard et al. 2012). Along this line, Mann et al. (2012) report an occurrence rate of super-Earths with periods lower than 50 days of $36 \pm 8\%$ around late-K to early M dwarfs.

The frequency of planets around M dwarfs seems to follow the same stellar mass and metallicity trends than FGK stars. That is, the frequency of gas-giant planets is a function of the stellar metallicity as well as of the stellar mass. On the other hand, the frequency of low-mass planets does not depend on the metallicity content or the mass of the stellar host (Bonfils et al. 2007; Johnson & Apps 2009; Schlaufman & Laughlin 2010; Rojas-Ayala et al. 2012; Terrien et al. 2012; Neves et al. 2013; Montet et al. 2014; Courcol et al. 2016; Maldonado et al. 2020). While most studies have focused only on the iron content or metallicity, in a recent work, Maldonado et al. (2020) show, for the first time, that there are no differences in the abundance distribution of elements other than iron between M dwarfs with and without known planets.

The detection of truly Earth twins via the Doppler technique requires a precision in the radial velocity measurements of the order of 0.1 ms^{-1} . While a new generation of ultra high-resolution spectrographs is coming to the fore (e.g. ESPRESSO Pepe et al. 2021), it is now clear that the major challenge to high Doppler precision is not the instrumental precision but the star itself. Stellar activity might produce line profile variations that skew the peak of a spectral line, leading to a velocity change in the star that can be (mis)-interpreted as Keplerian in nature. (Saar & Donahue 1997; Santos et al. 2000; Paulson et al. 2004; Wright 2005; Desort et al. 2007; Dumusque et al. 2011a). Some techniques such as an optimal schedule of the observations or the use of spectroscopic indicators of activity might be used to mitigate the effects of stellar oscillations, granulation or even the long-term activity (Dumusque et al. 2011a,b). However, the

short-term stellar activity (due to evolution and decay of active regions) has a characteristic timescale comparable with the stellar rotation period (e.g. Scandariato et al. 2017). Disentangling “true” keplerian signals from stellar variations is highly complex and requires the use of complementary and imaginative approaches like red-noise models, or Gaussian process regression (see e.g. Dumusque et al. 2017, and references therein).

Within the framework of the HARPS-n red Dwarf Exoplanet Survey (HADES) observing program (Affer et al. 2016) we have started the radial velocity monitoring of a large sample of low-mass stars (spectral types K7-M3). HADES main goal is to explore the frequency and formation conditions of small, potentially habitable planets around early-M dwarfs. The development of techniques to ensure the optimal outcome of the survey is an additional goal of HADES, and it includes target characterisation (Maldonado et al. 2015, 2020), optimal scheduling (Perger et al. 2017a), or detailed activity studies (Maldonado et al. 2017; Scandariato et al. 2017; Suárez Mascareño et al. 2018; González-Álvarez et al. 2019). HADES has already succeeded in discovering several super-Earth exoplanets, with masses ranging from $2.5 M_\oplus$ to $9 M_\oplus$ (Affer et al. 2016; Suárez Mascareño et al. 2017; Perger et al. 2017b; Pinamonti et al. 2018, 2019; Affer et al. 2019; Perger et al. 2019; Toledo-Adroán et al. 2021; González-Álvarez et al. 2021).

In this paper we present the discovery of a candidate super-Earth ($M_p \sin i \sim 9.65 M_\oplus$) planet orbiting around the early-M dwarf GJ 9689 with a period of 18.27 d. The detection of this planet has been challenging, as the proposed planetary period is very close to half the stellar rotation period (39.31 d). This fact makes the GJ 9689 b planet an interesting case of study. This paper is organised as follows. Section 2 reviews the stellar properties of GJ 9689. The spectroscopic data is presented in Sect. 3 while Sect. 4 describes the analysis of the radial velocity data. The origin of the radial velocity variations found in GJ 9689 is discussed at length in Sect. 5 where activity indicators, photometry, and CCF diagnostics are analysed. Section 6 describes the modelling of the radial velocity variations. The results are set in the context of planetary systems in Sect. 7. Our conclusions follow in Sect. 8.

2. The host star

GJ 9689 is an M0.5 dwarf located at a distance of 30.69 ± 0.01 pc (Gaia Collaboration 2020) from the Sun. Its main stellar properties are listed in Table 1. Basic stellar parameters (effective temperature, spectral type, mass, radius, surface gravity, and luminosity) are from Maldonado et al. (2020). They are computed following the procedures described in Maldonado et al. (2015)² which make use of the same spectra used in this work for the radial velocity analysis. In brief, effective temperatures and spectral types are determined from ratios of pseudo-equivalent widths of spectral features calibrated using stars with interferometric estimates of their radii and spectral-type standards. By studying a large sample of early-M dwarfs, Maldonado et al. (2015) also provide empirical calibrations for the stellar mass, radius, and surface gravity as a function of the stellar metallicity and effective temperature. Stellar metallicity is computed by a methodology based on the use of a principal component analysis and sparse Bayesian methods which also allows the determination of abundances of other elements different from iron³ (Maldonado et al. 2020). These parameters are listed for the whole

¹ <http://exoplanet.eu/>, as checked in December 2020

² <https://github.com/jesusaldonadoprado/mdslines>

³ https://github.com/jesusaldonadoprado/mdwarfs_abundances

HADES sample in Maldonado et al. (2017) and for a large sample of M dwarfs in current radial velocity searches in Maldonado et al. (2020).

Galactic spatial-velocity components (U , V , W) are computed from the radial velocities, together with *Gaia* parallaxes and proper motions (Gaia Collaboration 2020) following the procedure described in Montes et al. (2001) and Maldonado et al. (2010). GJ 9689 is classified as transition (thin/thick disk) star applying the methodology described in Bensby et al. (2003, 2005). No comoving objects seems to be present after carefully checking the available data in the *Gaia* EDR3 catalogue.

Table 1. Physical properties of GJ 9689

Parameter	Value	Notes
α (ICRS J2000)	20:13:51.8	
δ (ICRS J2000)	+13:23:20	
T_{eff} (K)	3836 ± 69	a
Spectral Type	M0.5	a
$[Fe/H]$ (dex)	0.05 ± 0.04	a
M_{\star} (M_{\odot})	0.59 ± 0.06	a
R_{\star} (R_{\odot})	0.57 ± 0.06	a
$\log g$ (cm s^{-2})	4.69 ± 0.05	a
$\log(L_{\star}/L_{\odot})$	-1.20 ± 0.09	a
$v \sin i$ (km s^{-1})	< 1.47	b
Age [†] (Gyr)	8.9 ± 3.9	a
π (mas)	32.5879 ± 0.0140	c
μ_{α} (mas/yr)	421.921 ± 0.014	c
μ_{δ} (mas/yr)	19.129 ± 0.015	c
v_{rad} (km s^{-1})	-67.701 ± 0.03	
U (km s^{-1})	-72.54 ± 0.02	
V (km s^{-1})	-42.24 ± 0.01	
W (km s^{-1})	-36.21 ± 0.02	
V (mag)	11.30	d
$(B - V)$ (mag)	1.365 ± 0.133	d
$(V - I)$ (mag)	1.60 ± 0.25	d
2MASS J (mag)	8.309 ± 0.029	e
2MASS H (mag)	7.633 ± 0.021	e
2MASS K _s (mag)	7.468 ± 0.021	e

Notes. (a) Maldonado et al. (2020); (b) Maldonado et al. (2017); (c) Gaia Collaboration (2020); (d) ESA (1997); (e) Cutri et al. (2003).

[†] By interpolation of parallaxes and stellar parameters within a grid of Yonsei-Yale isochrones, see (a) for details.

3. Spectroscopic observations

GJ 9689 has been observed during a period of almost seven and a half years, from BJD = 2456438 (May 26, 2013) to BJD = 2459130 (October 7, 2020). A total of 174 HARPS-N spectra were collected during this period. HARPS-N spectra cover the wavelength range 383–693 nm with a resolving power of $R \sim 115000$. Data were reduced using the latest version of the Data Reduction Software (DRS V3.7, Lovis & Pepe 2007) which implements the typical corrections involved in échelle spectra reduction, i.e. bias level, flat-fielding, order extraction, wavelength calibration, and merge of individual orders. RVs are computed by cross-correlating the spectra of the target star with an optimised binary mask (Baranne et al. 1996; Pepe et al. 2002). For GJ 9689 the M2 mask was used. This procedure is known to have several shortcomings starting from the fact that a symmetric analytical function is used to fit the asymmetric CCF. Furthermore, the spectra of an M dwarf suffer from heavy blends

resulting in side-lobes in the CCF that might affect the RV precision as well as the asymmetry indexes of the CCF (e.g. Rainer et al. 2020). In order to overcome these difficulties, RVs were also computed with the Java-based Template-Enhanced Radial velocity Re-analysis Application (TERRA, Anglada-Escudé & Butler 2012). TERRA measures the RVs by a least-square match of each observed spectrum to a co-added high signal-to-noise (S/N) template spectra derived from the same observations. We excluded from the analysis the bluest part of the spectra and only orders redder than the 22nd ($\lambda > 453$ nm) were considered (note that HARPS-N spectra have a total of 66 échelle orders).

4. Radial velocity time series analysis

Figure 1 (top) shows the RV (derived with the TERRA pipeline) time series of GJ 9689. The RV data show a rms of 4.59 m s^{-1} , approx. 3 times the mean error of the measured RVs (1.55 m s^{-1}) when the TERRA pipeline is used. If the RV data are derived by the DRS then we obtain a rms of 5.35 m s^{-1} while the mean error of the measured RVs is 2.94 m s^{-1} .

In a recent work, Perger et al. (2017a) perform a detailed comparison on the accuracy of the TERRA and DRS pipelines using the HADES spectra collected so far. Under the assumption that smaller rms of the RV measurements correspond to smaller RV noise rms, the authors conclude that TERRA RVs should be preferred. In particular, for GJ 9689, the rms of the RV measurements obtained with TERRA is around 1 m s^{-1} lower than the value derived by the DRS RVs. The analysis presented in the following refers to TERRA RVs.

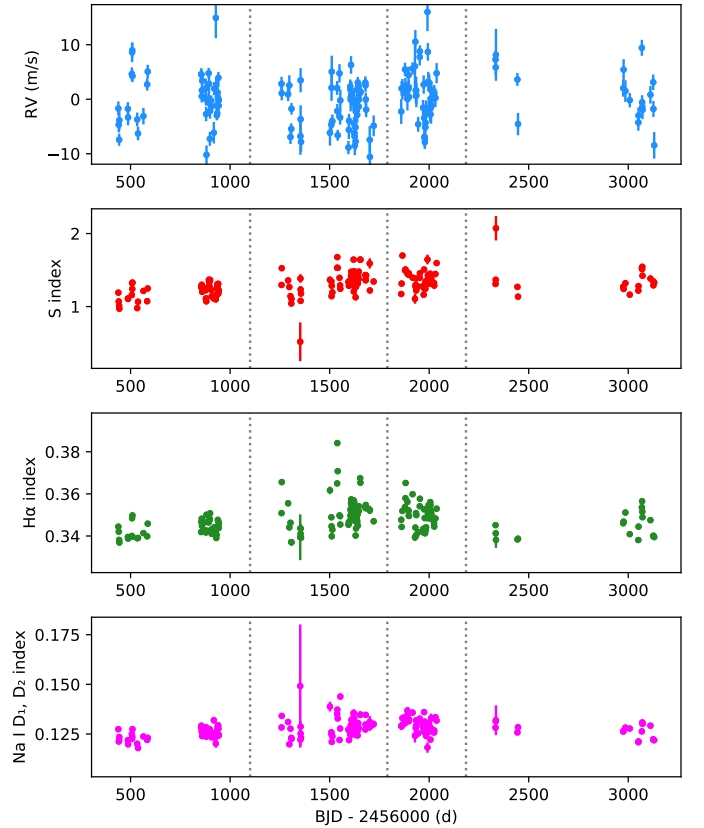


Fig. 1. From top to bottom: Original radial velocity (derived with the TERRA pipeline), S-index, $H\alpha$ -index, and Na I D₁, D₂-index time series for GJ 9689. Vertical dotted lines indicate the first three observing seasons as used in our study.

A search for periodicities in the RV data was performed by using the generalised Lomb-Scargle periodogram (GLS, Zechmeister & Kürster 2009). The periodogram, see Figure 2, identifies two significant frequencies. The peaks are found at $0.054734 \pm 0.000039 \text{ d}^{-1}$ (period of $18.27 \pm 0.01 \text{ d}$), and $0.025436 \pm 0.000059 \text{ d}^{-1}$ which corresponds to a period of $39.31 \pm 0.10 \text{ d}$. In order to test the significance of these frequencies a bootstrapping analysis was done. A series of 10^4 simulations was performed. In each simulation the dates of the observed RVs were kept, but random RVs were constructed from the original ones, by drawing random values from normal distributions with means equals to the RV value and σ equal to the RV error. Then, the simulated RVs were randomly shuffled. The false alarm probability (FAP) of a given period is obtained as the fraction of simulated periodograms in which a peak with a periodogram power larger than the original period's power is found (e.g. Endl et al. 2001). Both signals are found to have a FAP below the 0.1% threshold.

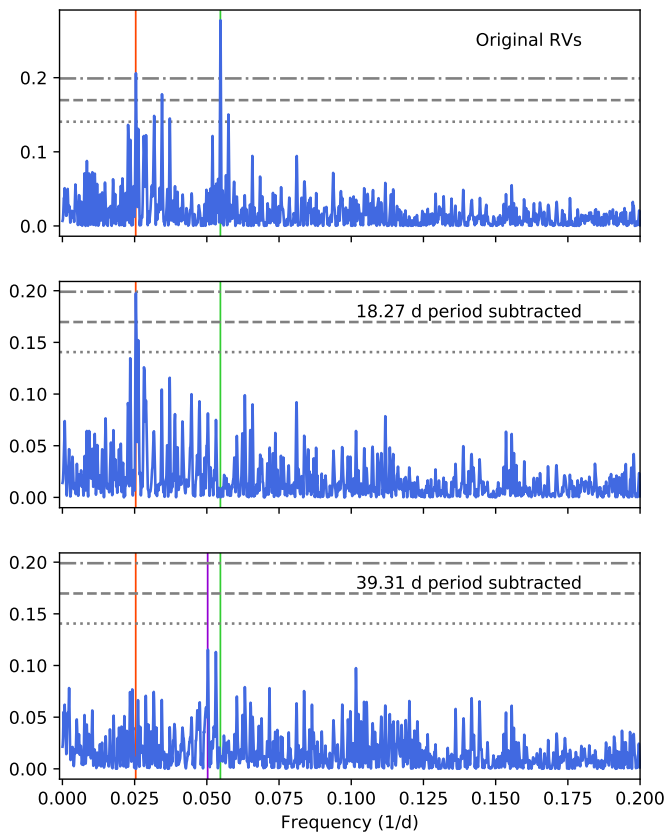


Fig. 2. Top: GLS periodogram of the TERRA RV measurements. Middle: GLS periodogram after subtracting the 18.27 d period. Bottom: GLS periodogram after subtracting the 18.27 and the 39.31 d signals. Values corresponding to a FAP of 10%, 1%, and 0.1% are shown with horizontal grey lines. The vertical red line indicates the period at 39.31 d while the vertical green line shows the 18.27 d period. The first harmonic of the 39.31 d signal is shown in violet.

We performed a search for additional periods by subtracting in a sequential way the most prominent period until no significant signal is left, a procedure usually known as prewhitening. First of all, a sinusoidal function with period 18.27 d was fitted and subtracted. It can be seen from the periodogram, Figure 2 (middle panel), that the period at 39.31 d is still significant after the removal of the 18.27 d signal. Once the 39.31 d signal is also subtracted, no significant periods remain in the periodogram analysis, Figure 2 (bottom panel). We note that the peak with the

highest power seems to be the harmonic of the 39.31 d signal, as it is located at a frequency of $0.050364 \pm 0.000075 \text{ d}^{-1}$, which corresponds to a period of $19.86 \pm 0.03 \text{ d}$.

We note that if the 39.31 d signal is firstly prewhitened from the raw RV dataset, then the 18.27 d signal clearly remains, Figure 3. That suggests that both signals are not connected.

For the sake of completeness we also show the GLS periodogram derived using the DRS RVs in Figure B.1, finding similar results.

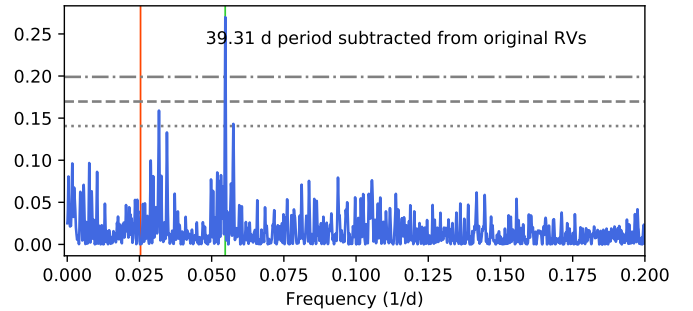


Fig. 3. GLS periodogram when the 39.31 d signal is subtracted from the original RV measurements. Values corresponding to a FAP of 10%, 1%, and 0.1% are shown with horizontal grey lines. The vertical red line indicates the period at 39.31 d while the vertical green line shows the 18.27 d period.

5. Origin of the radial velocity variations

5.1. Activity indexes

In order to disentangle the effects of activity in the measured RVs from other possible effects we made use of several spectroscopic indicators of chromospheric activity, the Ca II H & K (S-index), H α , and Na I D₁, D₂ lines. Although these quantities are provided by the TERRA pipeline, the H α , and Na I activity indexes came without uncertainty measurements. Therefore, we decided to measure the activity indexes following the definitions provided by Gomes da Silva et al. (2011, 2018).

Figure 1 shows the temporal variation of the different activity indexes while the periodogram analysis is given in Figure 4. A long-term activity trend in the three time series is seen. The trend has a period of $\sim 34500 \text{ d}$, 20400 d , and 56500 d , in S-index, H α , and Na I index, respectively, suggesting an activity cycle of more than 55 yrs⁴. Note that these periods are much longer than the observation timespan, so they are extremely uncertain. Once the long-term activity trend is subtracted by a sinusoidal fit, a group of peaks with periods in the range 35–45 d is found in all the activity indexes. The highest peaks are located at $35.55 \pm 0.05 \text{ d}$ (S-index), $39.27 \pm 0.03 \text{ d}$ (H α -index), and $42.54 \pm 0.10 \text{ d}$ (Na I-index). A clear peak close to the RV signal at 39.31 d is found in the three indexes.

Our analysis also shows that there is a peak close to 18.27 d in the S-index although it is not significant. No significant peaks seem to be present at 18.27 days neither in the H α -index, nor in the Na I-index.

As an additional test we checked whether our derived RVs show any correlation with the activity indexes finding no significant correlation between these quantities. The corresponding plots are shown in Fig. 5. For the S-index the Spearman's rank

⁴ For the Na I index analysis, one observation was excluded due to its large uncertainty.

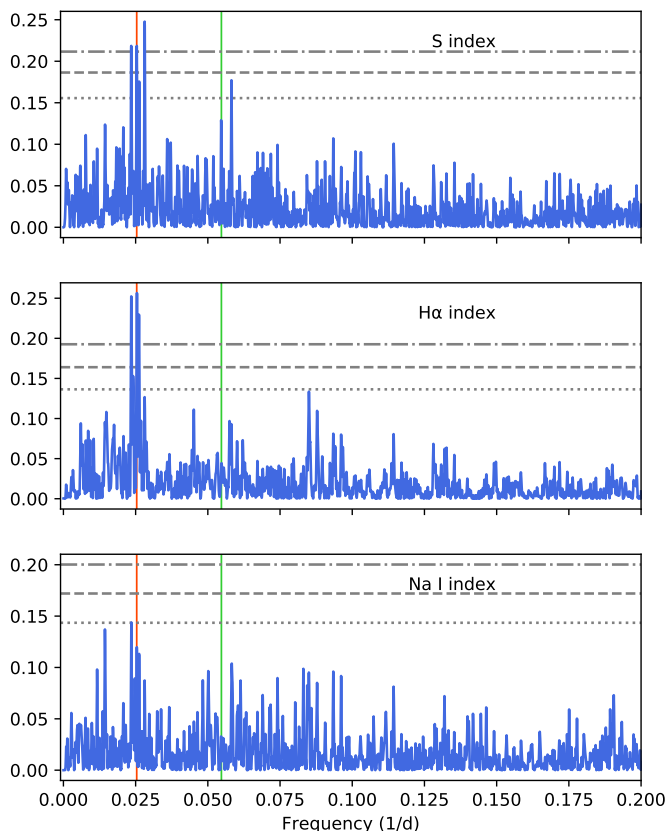


Fig. 4. From top to bottom: GLS periodogram of the S, H α , and Na I activity indexes after the subtraction of the long-term activity trend. The vertical red line indicates the RV period at 39.31 d while the vertical green line shows the RV period at 18.27 d. Values corresponding to a FAP of 10%, 1%, and 0.1% are shown with horizontal grey lines.

ρ is 0.1890 ± 0.0752 with a z-score = 1.058 ± 0.431 while for RVs and H α -index we obtain $\rho = 0.1214 \pm 0.0772$ and z-score = 0.675 ± 0.433 . If the activity indexes are corrected by the long-term activity trend, we then obtain $\rho = 0.2384 \pm 0.0756$ and z-score = 1.346 ± 0.4444 for the S-index, and $\rho = 0.2283 \pm 0.0756$ and z-score = 1.286 ± 0.441 for the H α -index. The statistical tests were performed by a bootstrap Monte Carlo simulation plus a Gaussian random shift of each data point within its error bars (Curran 2014)⁵.

Finally, we also computed the autocorrelation function (ACF) for the RVs, S-index, and H α indexes. The corresponding plots are shown in Fig. B.2 (left). The ACF function has been computed following the prescriptions given by Edelson & Krolik (1988), using a python wrapper developed by Robertson et al. (2015). It is clear that the three datasets show a periodicity around ~ 40 d. But the plot also shows that only in the RV data there is another periodicity at ~ 20 d. In order to confirm that, we also computed the GLS periodogram of the ACFs, Fig. B.2 (right). While in the RV dataset the periods at ~ 18.27 and 39.31 d are clearly visible, the ACF function of the activity indicators do show only the period at 39.31 d. We note that the ACF of the H α index shows a peak around 17.3 d, but it is not statistically significant (indeed, there is a more significant period at ~ 11.8 d).

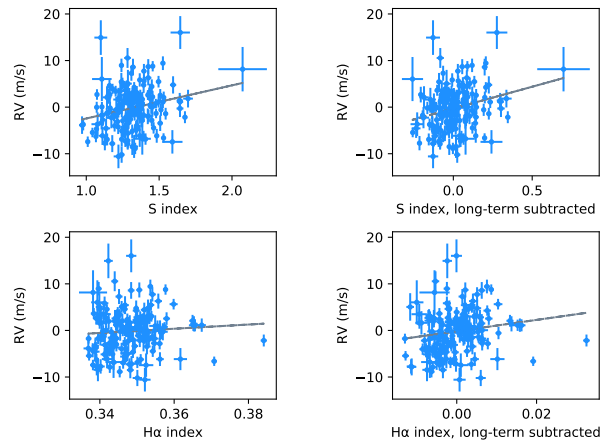


Fig. 5. Activity indexes vs. radial velocities. Top left: S-index. Top right: S-index after the subtraction of the long-term activity trend. Bottom left: H α -index. Bottom right: H α -index after the subtraction of the long-term activity trend. The grey line shows the best linear fit.

5.2. Periodogram power as a function of time

Another way to disentangle RVs variations due to the presence of planets from stellar activity is to study the evolution of the periodogram power of the RVs periods as a function of the number of observations (e.g. Affer et al. 2016; Mortier & Collier Cameron 2017). Activity regions change in shape and position with time, thus producing incoherent (in amplitude and phase) signals. In the periodograms this incoherency translates into wider peaks and/or a bunch of peaks aside the central one. On the other hand, a keplerian signal gains in power with time, thanks to its coherency.

Figure 6 shows the variation of the periodogram power as a function of the number of observations for the periods found in the RVs time series. For this exercise we use the Bayesian generalised Lomb-Scargle periodogram (BGLS, Mortier et al. 2015) which computes the relative probability between peaks.

The analysis reveals that even at a relatively low number of observations, around 35–40, a period between 18 and 19 d is visible. At around ~ 110 observations the period is well stabilised at ~ 18.27 d and since then, it remains constant in period and logPrb (Fig. 6, left).

The analysis also reveals a signal at a period slightly larger than 40 d (although at a rather modest probability), however, this signal disappears at around 30 observations. It is likely the ~ 39 d signal but not well constrained due to the low number of observations. A new period around 39 d appears again when the number of observations is around 80. The period of this signal is not well-constrained and it is worth noticing that it is accompanied by many other signals (Fig. 6, right).

5.3. Photometry

5.3.1. EXORAP photometry

GJ 9689 was observed photometrically within the EXORAP (EXOplanetary systems Robotic APT2 Photometry) program from MJD = 56783 d to MJD = 58034 d. Observations were carried out at the Serra la Nave observatory on Mt. Etna (Italy) using a 80-cm f/8 Ritchey-Chretien robotic telescope (Automated Photoelectric Telescope, APT2). A total of 203, 201, 202, and 209 observations were obtained in the photometric bands B, V,

⁵ <https://github.com/PACurran/MCSpearman/>

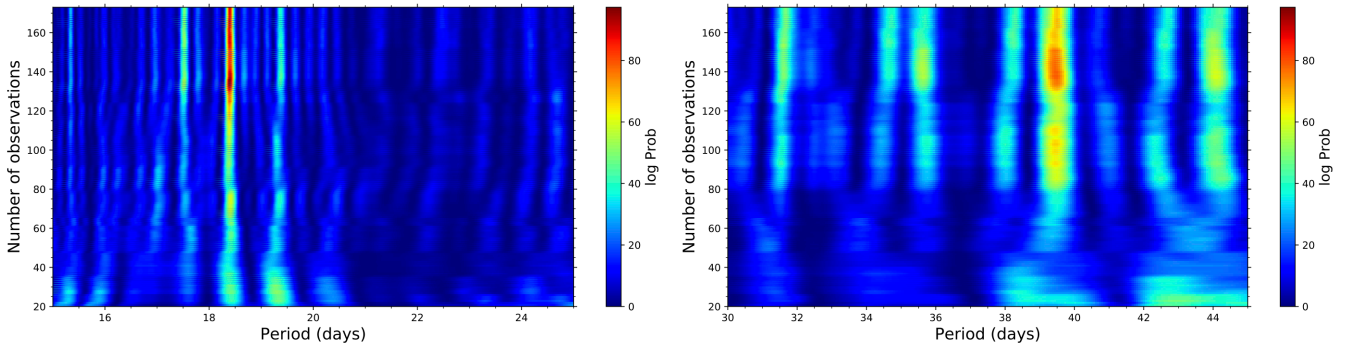


Fig. 6. Stacked-BGLS periodogram of the HARPS-N RV data of GJ 9689. Left: zoom around the 15 - 25 d region. Right: zoom around the 30 - 45 d region.

R, and I, respectively. Figure 7, panels (a) to (d), shows the corresponding light curves.

A search for periodicities reveals the presence of a long term signal with periods of ~ 244 d (B), ~ 256 d (R), ~ 270 d (I). No long-term trend is found in band V. Once these long-term trends are subtracted, the corresponding GLS analysis, Figure 8 panels (a)-(d), reveals the presence of several signals with periods between ~ 35 and 39 days. The highest periods are found at 34.87 ± 0.15 d (B), 38.51 ± 0.16 d (V), 38.85 ± 0.16 d (R) and 34.97 ± 0.18 d (I). The significance of these peaks is better than 0.1% in bands B, V, and R, but slightly lower than 10% in band I. The periodograms of the V and R bands (Figure 8 panels (b) and (c)) also show some amount of power in the region around 18 days. However, no clear peaks are found at 18.27 days.

A comparison of Fig. 1 and Fig. 7 shows that the star is brighter when the activity S-index is lower. This behaviour is quite different from what we observe in the Sun (and similar stars) where long-term variability is dominated by faculae. We thus speculate that the stellar activity in GJ 9689 is spot-dominated (Radick et al. 2018).

5.3.2. APACHE photometry

The APACHE (A Pathway toward the Characterisation of Habitable Earths) photometric survey (Sozzetti et al. 2013) observed GJ 9689 with a 40-cm telescope located in the Astronomical Observatory of the Autonomous Region of the Aosta Valley. The observations cover a time span of 122 days from HJD = 2456445 d to HJD = 2456567 d. The number of observations amounts to 158. A Johnson I filter was used to carry out the observations. A clear significant period is found at 38.22 ± 1.04 d in the GLS analysis.

Note that APACHE and EXORAP I datasets have different sampling, baselines, and data quality so it is not surprising to find slightly different periodograms. In particular the EXORAP dataset covers a baseline of ~ 1250 d, allowing us the detection of a long-term signal (~ 270 d) while the APACHE baseline is only 122 d.

5.3.3. Hipparcos H band photometry

We also analysed the available HIPPARCOS (ESA 1997) H band photometry. GJ 9689 was observed during 975 days between BJD = 2447964 d and BJD = 2448939 d, with a total of 101 data points. The corresponding periodogram is shown in panel (f) of Figure 8, where no significant periods are found. While it is true that a peak seems to be present at ~ 18 d, it is very far from

being significant. Furthermore, this region of the periodogram is largely crowded with numerous peaks with a similar (or larger) power.

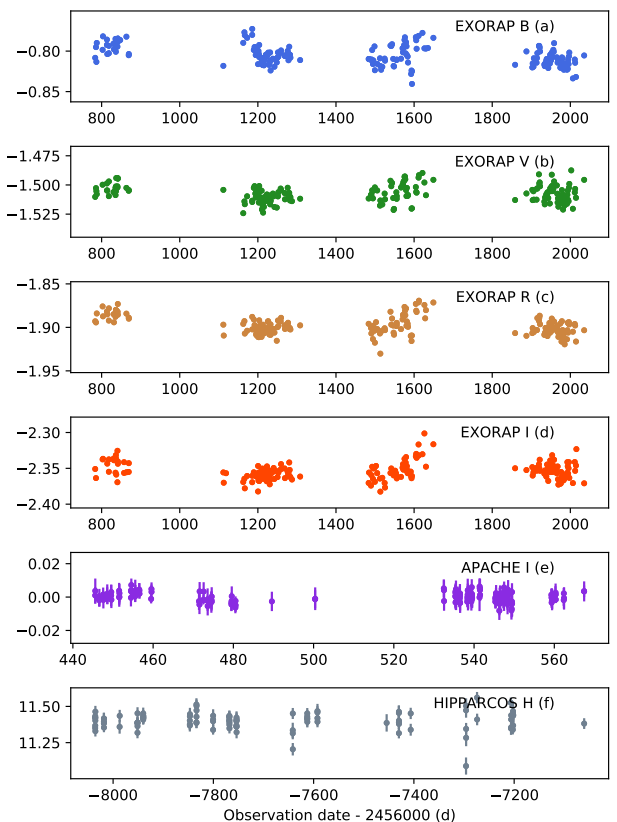


Fig. 7. Original photometry time series: (a) EXORAP B, (b) EXORAP V, (c) EXORAP R, (d) EXORAP I, (e) APACHE I, (f) HIPPARCOS H. Note that the observations are not contemporaneous. For EXORAP observation dates are in JD, for APACHE in HJD, while for HIPPARCOS observation dates are in BJD.

5.4. Wavelength dependence

We also explored the dependence of the periodic signals identified in the RV analysis on the wavelength. In order to do that we proceeded as in Tuomi et al. (2013) and exploited the fact that the TERRA pipeline allows us to select a blue cut-off aperture when computing the RVs. The results are shown in Figure 9 that shows the GLS periodogram of the RVs obtained by using dif-

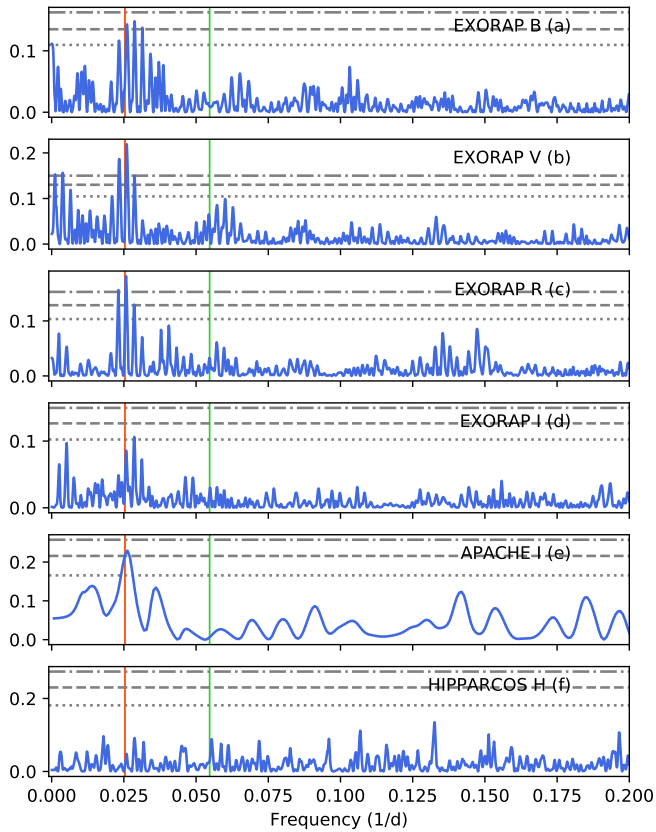


Fig. 8. GLS periodograms of the photometry data sets. Panels (a), (c), and (d) show the EXORAP B, R, and I band photometry after subtracting the corresponding long term periods (see text for details). Panels (b), (e), and (f) show the original (i.e. no long term period subtracted) EXORAP V, APACHE I and HIPPARCOS H photometry analysis. Values corresponding to a FAP of 10%, 1%, and 0.1% are shown with horizontal grey lines. The vertical red line indicates the period at 39.31 d while the vertical green line shows the 18.27 d period.

ferent blue cut-off wavelengths. It can be seen that the period at 18.27 days is always visible, independently of the bluest échelle aperture used in the RVs computations. On the other hand, the period at 39.31 days disappears when only wavelengths redder than ~ 600 nm are used in the RVs computation (two bottom panels).

5.5. CCF Asymmetry diagnostics

Stellar spots and pulsations are known to affect the shapes and the centroids of the spectral lines. We therefore investigated for possible correlations between the RVs and several CCF asymmetry diagnostics, namely the CCF width (FWHM) and its bisector velocity span (BIS) (e.g. Queloz et al. 2001; Boisse et al. 2009; Queloz et al. 2009). Both quantities are directly provided by the HARPS-N DRS. As mentioned before, these quantities should be taken with caution when dealing with low-mass stars. Figure 10 (upper panels) shows the TERRA RVs as a function of the FWHM and BIS values. A Spearman's correlation test confirms that there is no monotone dependence between the RVs and the measured FWHM values ($\rho = -0.1304 \pm 0.0807$ and z-score = -0.726 ± 0.454) or between the RVs and the BIS ($\rho = 0.0315 \pm 0.0781$ and z-score = 0.174 ± 0.433). Furthermore, no significant signals were found in the periodogram analysis of the BIS. For the FWHM, a rather broad but statically significant period is

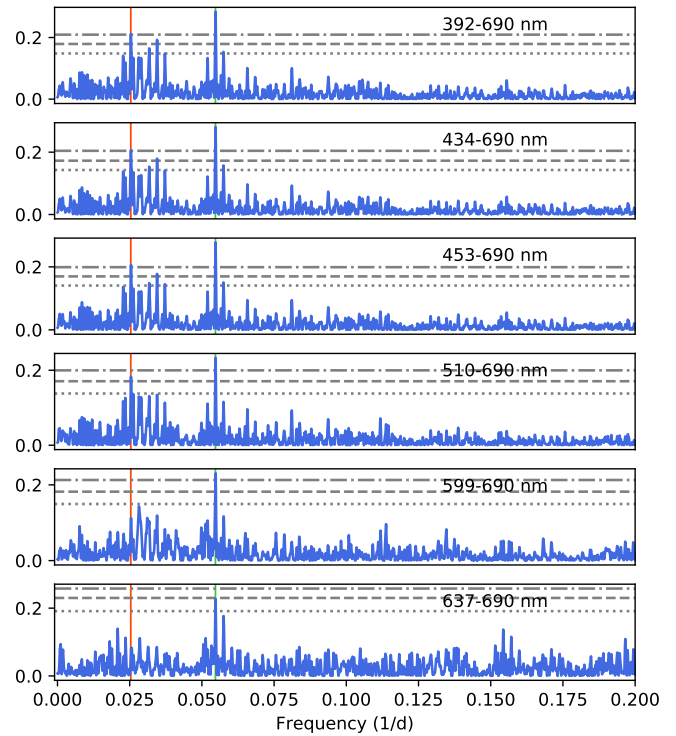


Fig. 9. GLS periodograms of the TERRA RVs as a function of the blue cut-off wavelength. From top to bottom: RVs are computed using the 1, 16, 22, 37, 55, and 61 aperture as blue cut-off. Values corresponding to a FAP of 10%, 1%, and 0.1% are shown with horizontal grey lines. The vertical red line indicates the period at 39.31 d while the green line shows the 18.27 d period.

found at $\sim 402 \pm 8$ d, but no significant periods remain after this period is prewhitened. No signals are found either in BIS or in FWHM around the periods identified in the RV analysis.

Given that TERRA RVs are derived using a different method (and a different pipeline), a comparison between the FWHM and BIS values with the RVs derived by the CCF performed by the HARPS-N DRS is also mandatory. The corresponding plots are shown in Figure 10 (bottom panels). We find that the results are similar to the ones obtained using the TERRA RVs, that is, there is no dependence between the DRS RVs and the measured FWHM or BIS values ($\rho = -0.2990 \pm 0.0732$ and z-score = -1.712 ± 0.446 for the FWHM, and $\rho = -0.0087 \pm 0.0797$ and z-score = -0.048 ± 0.443 for the case of the BIS).

5.6. Analysis of individual seasons

In this section we analyse the data by considering three different observing seasons. They are indicated with vertical lines in Fig. 1. Note that 'season 1' and 'season 2' do indeed contain data from two observing seasons. This choice was made in order to have enough RV data points in each season. The first season includes 46 data points taken from May 26, 2013, to October 22, 2014. The second season covers the observations performed between August 23, 2015 and November 28, 2016 with 62 observations. Finally, we consider 47 observations between April 16, and October 10, 2017. The remaining observations are not considered as they are sparse in time and amount only up to 19.

The RV and S-index periodogram for each season are shown in Fig. 11 (left, and right, respectively). The vertical red and green line indicate the identified periods at 39.31 d and 18.27 d,

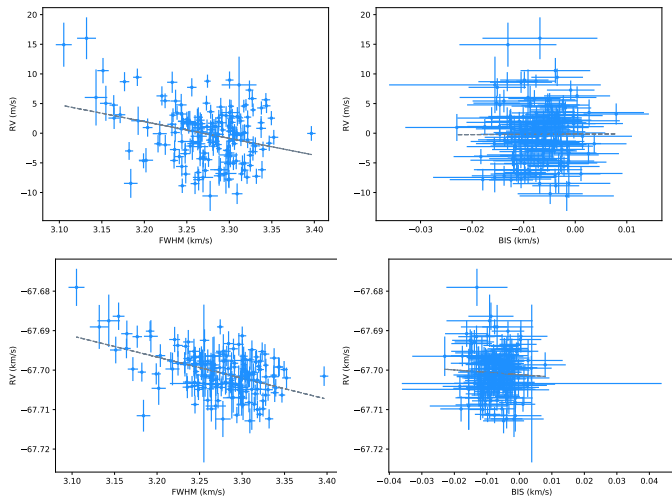


Fig. 10. CCF asymmetry diagnostics vs. radial velocity. Left, FWHM. Right, BIS. The grey line shows the best linear fit. Upper panels show the TERRA RVs, while bottom panels show the results for the DRS RVs.

respectively. The figure clearly shows that the RV period at 18.27 d is visible in all seasons, with a similar structure and power. However, the structure of the RV period at 39.31 d changes from one season to another. The peak is located at 38.53 d, 39.25 d, and 35.93 d in the first, second, and third season, respectively. Its power also changes with time, being the dominant signal in the second and third seasons. We note that in these seasons, the values of the S-index are higher than in the first season (see Fig. 1), supporting the hypothesis that the ~ 39.31 d period is due to stellar activity. Regarding the S-index (right panel), there are no signals close to 18.27 d in any of the seasons, while there are prominent signals close to 39.31 d in all seasons. The structure of these signals change from one season to another and the highest periods are located at 42.56 d, 40.76 d, and ~ 178 d in the first, and second, and third season, respectively.

5.7. Spectral window analysis

Given that the periods found in the RV time series of GJ 9689 are at 18.27 d and 39.31 d it is reasonable to ask whether the signal at 18.27 d is the first harmonic of the signal at 39.31 d.

To answer this question, Figure 12 (top panel) shows the spectral window of the original RV dataset of GJ 9689. There are three prominent peaks at frequencies 0.000854 d^{-1} , 0.001895 d^{-1} , and 0.002749 d^{-1} . These peaks are related to the gaps in the RV curve (Fig. 1). There is the obvious 1 cycle/year peak (0.00275 d^{-1}) and two peaks related to the poor sampling in the 2458000 - 2459100 BJD interval: 1 cycle/1100 d (0.0009 d^{-1}) and 1 cycle/550 d (0.0018 d^{-1}). The presence of a peak in the spectral window at 0.001895 d^{-1} might indicate an alias phenomenon as $0.001895 \text{ d}^{-1} + 0.025436 \text{ d}^{-1}$ (frequency of the 39.31 d period) is 0.027331 d^{-1} , which is close to $0.054734/2 \text{ d}^{-1}$ ($\approx 0.027367 \text{ d}^{-1}$, i.e., half the frequency of the 18.27 d period).

To further investigate this possibility, we also analysed the spectral window in the three different seasons considered before. The results are shown in Fig. 12 where for each season we indicate with a magenta line the position that a peak in the spectral window should have in order to produce the aliasing phenomenon between the 39.31 d and 18.27 d periods. The analysis takes into account that the signals appear at slightly different frequencies in the different seasons. For example, in season one, the

39.31 d signal appears at 38.53 d ($f = 0.025953 \text{ d}^{-1}$) while the 18.27 d signal is at 18.24 d ($f = 0.045823 \text{ d}^{-1}$). If the 38.53 d and 18.27 d were related by an alias phenomenon due to a signal in the window function, this signal should appear at a frequency $f_{\text{win}} \approx 0.001458 \text{ d}^{-1}$. As it can be seen in Fig. 12 (second panel from top), there is no such a signal in the window function of season one. The same happens in the second season (third panel from top). In this case, the 39.31 d signal appears at 39.24 d ($f = 0.02548 \text{ d}^{-1}$) and the 18.27 d at 18.14 d ($f = 0.055122 \text{ d}^{-1}$). If the signal at 18.14 d were an alias of the 39.24 d signal, there should be a signal in the window function at a frequency $f_{\text{win}} \approx 0.0021 \text{ d}^{-1}$, which is not the case. In the third season (bottom panel) the signals are located at 35.93 d ($f = 0.027835 \text{ d}^{-1}$), and 18.71 d ($f = 0.053457 \text{ d}^{-1}$). Again, there are no peaks in the spectral window that might originate an aliasing phenomena.

We conclude that it is unlikely that the 18.27 d signal is the harmonic of the 39.31 d, a result which is in line with all the different analyses performed before.

6. Modelling of the radial velocity variations

The analysis performed in the previous section is consistent with a keplerian origin of the coherent signal at 18.27 d, while the incoherent signal at 39.31 d seems to be related to the rotation period of the star. This conclusion is based on the following observational facts:

- A periodicity close to 39.31 d is found in the analysis of the main optical activity indicators as well as in the analysis of the available photometry.
- Its power and frequency changes with the number of observations and from one observing season to another.
- This signal tends to disappear if only the reddest region of the spectra is used for the computation of the RVs.

On the other hand, for the 18.27 period:

- It does not seem to be related (to be a harmonic) of the 39.31 days period.
- No hint of this period is found in the activity indexes, photometry, or CCF asymmetry indicators.
- It appears in all observing seasons at a similar frequency and similar power. In addition, it does not show variations with the number of observations.
- It is always found in the RVs analysis even if only the reddest region of the spectra is considered.

6.1. Gaussian processes modelling

In order to model the RV data we have defined a Bayesian framework based on a Monte Carlo sampling of the parameter space with a Gaussian Processes model (GP). Before modelling, a 3σ clipping algorithm was applied to the RVs to identify potential outliers that might affect the results. As a consequence, two data points were excluded from the following analysis. The likelihood function is given by

$$\ln p(y_n, t_n, \sigma_n^2, \theta) = -\frac{1}{2} \mathbf{r}^T \mathbf{K}^{-1} \mathbf{r} - \frac{1}{2} \ln \det \mathbf{K} - \frac{N}{2} \ln 2\pi \quad (1)$$

where y_n , t_n , σ_n are, respectively, the radial velocities, time of observations and errors, θ is the array of parameters, \mathbf{r} is the residual vector obtained by removing the (deterministic) model

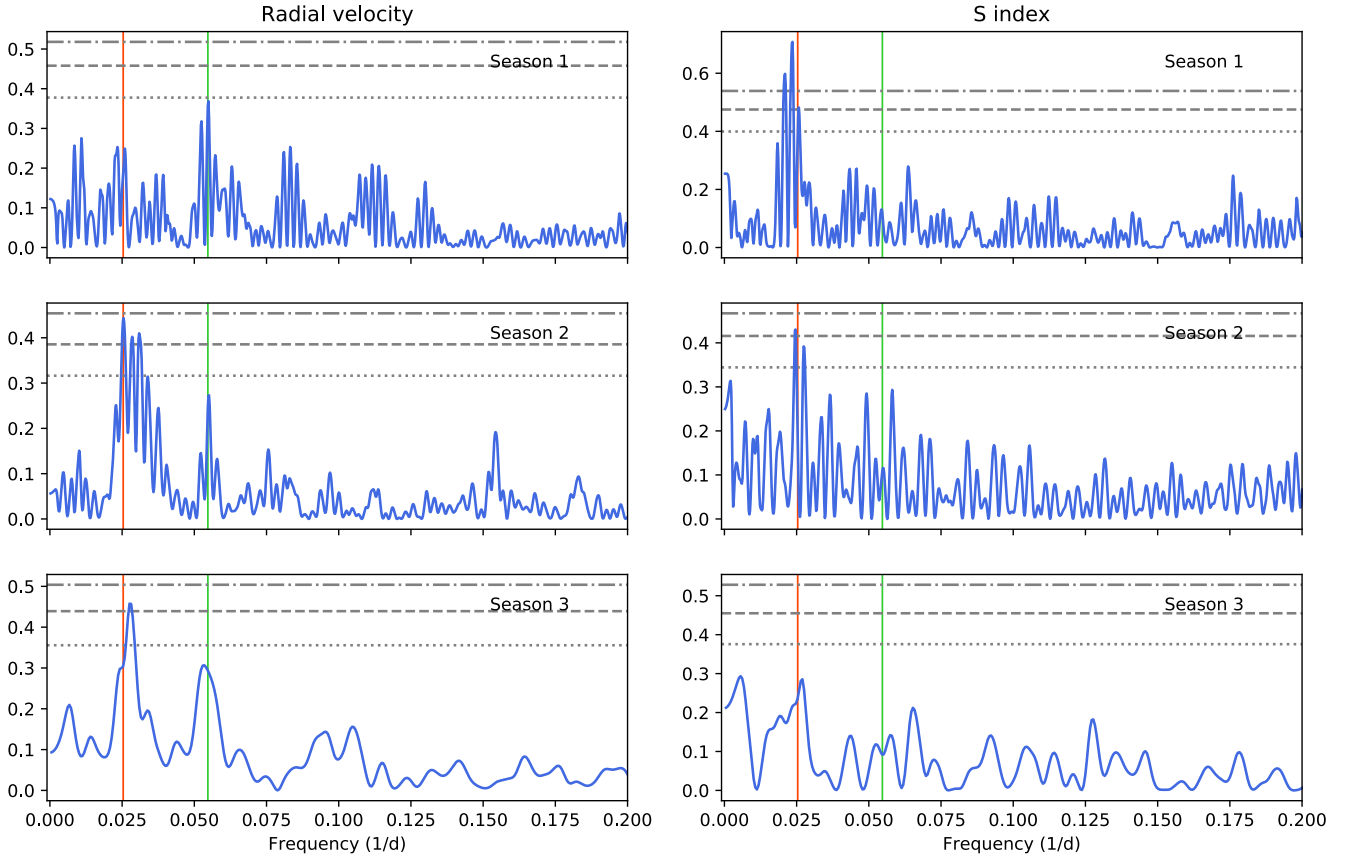


Fig. 11. GLS periodograms for the different seasons analysed. Left: RVs. Right: S-index. Values corresponding to a FAP of 10%, 1%, and 0.1% are shown with horizontal grey lines. The vertical red line indicates the period at 39.31 d while the vertical green line shows the 18.27 d period.

from data, K is the covariance matrix and N is the number of observations.

The covariance (or kernel) function adopted in this analysis is a Quasi-Periodic (QP) function and it has been obtained by multiplying an exp-sin-squared kernel to a squared-exponential kernel (george python package, Ambikasaran et al. 2014) added to an extra white noise (jitter) term, and it is defined as follows

$$k(i, j) = h^2 \exp\left(-\frac{(t_i - t_j)^2}{2\tau^2}\right) \exp\left(-\frac{\sin^2(\pi(t_i - t_j)/P_{rot})}{2\omega^2}\right) + \delta_{ij}\sigma_{Jit} \quad (2)$$

where $k(i, j)$ is the ij element of the covariance matrix, t_i and t_j are two times of the RV data set, h is the amplitude of the covariance, τ is the timescale of the exponential component, ω is the weight of the periodic component, P_{rot} is the period, δ_{ij} is the Kronecker delta function and σ_{Jit} is the white noise term.

The parameter space is sampled with *emcee* (Foreman-Mackey et al. 2013), based on the affine-invariant ensemble sampler for Markov chain Monte Carlo (MCMC) (Goodman & Weare 2010).

In this analysis we have compared two models which differ on the presence of a planetary (keplerian) signal (Fulton et al. 2018) but share the effect of a linear trend (characterised by the parameters γ , and $\dot{\gamma}$), respectively, 'GP-only' and 'Star-planet' models.

Priors of the models are reported in Table 2, they have been chosen uninformative and as large as possible. This parameter space is covered by 32 walkers, randomly initialised within the

priors ranges. This choice on the initial position of the walkers produces very low probability values at the beginning of the *emcee* chain. These values have been eliminated by a burn-in phase, here set as the first 20K steps. After the burn-in phase a blob, centred at the maximum probability position, is initialised to feed a following chain. This chain runs until the autocorrelation time of each parameter (see Sokal 1996), evaluated every 10K steps, varies less than 1% and the chain is 100 times longer than the estimated autocorrelation time. With this definition of convergence, chains converged after 120K and 270K steps, respectively, for the model 'GP-only' and 'Star-Planet' models.

The resulting posterior distributions are presented, respectively, in Fig. 13 and Fig. 14. As an estimate of the goodness of the model, we have calculated the Bayesian Information Criterion (BIC), defined as follows

$$BIC = k \ln(N) - 2 \ln(\mathcal{L}) \quad (3)$$

where k is the number of model parameters, N the number of data points and \mathcal{L} the maximum likelihood of the model. We obtain that there is strong evidence in supporting the 'Star-planet' model (BIC=912.4) against the 'GP-only' model (BIC=930.9) because the BIC difference is more than 10 (Kass & Raftery 1995). Figure 15 shows the best-fit 'Star-planet' model (top), the corresponding RV residuals (middle), and the RV curve folded at the best-fit orbital period for the detected planet (bottom). The best-fit parameters are listed in Table 2. Given that the derived eccentricity is not statistically significant, we also provide the 68% upper limit. We attempted a 'Star-planet' model with zero eccentricity. The corresponding BIC value is almost identical to the eccentric model.

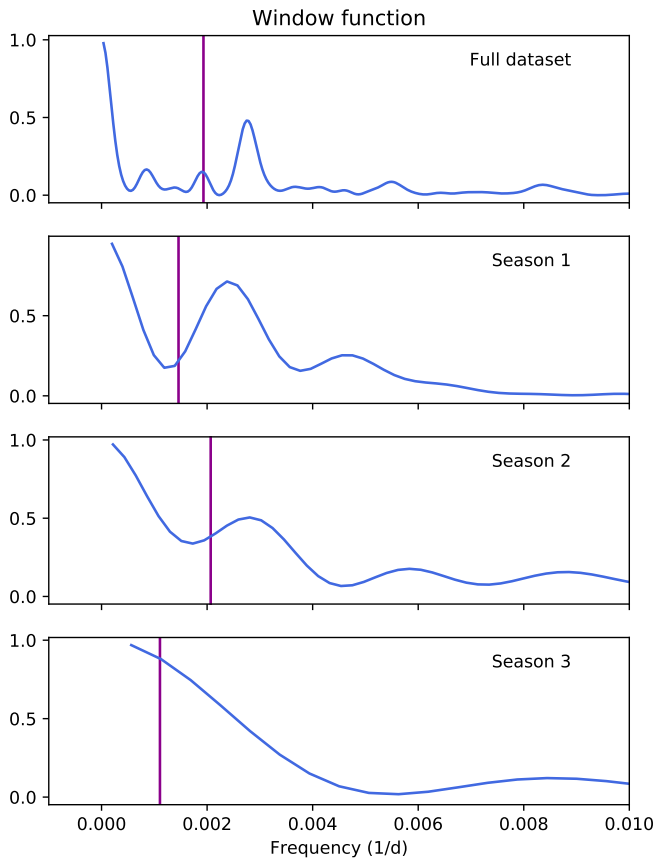


Fig. 12. Spectral window when the full RV dataset is considered (top) and for each of the different analysed seasons. The magenta line indicates the frequency that a signal in the spectral window should have in order to produce an aliasing phenomenon between the ~ 18.27 d and ~ 39.31 d periods.

In order to test whether the GP part of the model can generate a spurious signal at ~ 18 d, we derive a FAP-like significance of the ~ 18 d signal by drawing a sample of 10^4 RV curves from the ‘Star-planet’ model using the best fit parameters but excluding the planetary part. Then, we counted how many samples have the power of the ~ 18.27 d signal greater than the value obtained by evaluating the periodogram on the original RV data. This condition was never achieved.

As a further investigation, we have also checked on the stability of the planetary signal by applying the same GP analysis with the ‘Star-planet’ model to the seasons defined in Sect. 5.6. In this case we set the burn-in phase to 50K steps and we have run the second chain until it reaches 100K steps.

Due to the small amount of points in each season, we have shortened the prior ranges of the kernel and the linear trend parameters within 1σ from the median of the posterior distributions presented in Fig.14. For the same reason the orbital period is constrained within 3σ while the other prior ranges are unchanged with respect to the previous analysis. The result of this analysis is presented in Table 3. Note that in all seasons we derive the same planetary parameters (within the uncertainties) which shows that the Keplerian signal is coherent in all seasons.

As an additional test on the stability of the planetary signal, we analyse how the RV semi-amplitude varies as a function of the number of observations. The results are shown in Fig. 16 where it can be seen that starting from ~ 85 observations the value of K_b remains constant within the uncertainties around a

value of 3.5 ms^{-1} . Note that for this exercise we run the ‘Star-planet’ model with the priors as listed in Table 2 and run the second chain until it reaches 100K steps.

For the sake of completeness, we tested a model with a second additional planet. Given that the RV time-series analysis reveals no more addition signals to the ones already discussed, we performed a blind search, using a wide prior for the period of the second planet. More specifically, we tested a model with a second planet with a period between 1 d and 100 d, between 100 d and 200 d, and between 200 d and 300 d. None of these models provide a lower BIC than the ‘One planet - star’ model, confirming that, if there are more planets in the system, they are difficult to reveal with the data at hand.

We also run the ‘Star-planet’ model using the quasi-periodic with cosine (QPC) kernel defined in Perger et al. (2021). The QPC kernel is defined as an QP kernel but it adds an additional term in order to account for the $P_{\text{rot}}/2$ peaks in the autocorrelation function. The corresponding results are given in Table 3. It can be seen that the best obtained values are almost identical to the ones derived using the QP. The QPC has a BIC value of 917.6, which is slightly larger than the value obtained using the QP kernel (BIC = 912.4).

As a final test, we also explored the full (hyper)-parameter space using the publicly available Monte Carlo (MC) nested sampler and Bayesian inference tool MULTINEST v3.10 (e.g. Feroz et al. 2019), through the pyMULTINEST wrapper (Buchner et al. 2014). MULTINEST is known to provide accurate estimates of the Bayesian evidence \mathcal{Z} , that can be used to perform a statistical comparison between different models. To test the planetary nature of the ~ 18 day signal (circular orbital approximation), we fitted the RVs using two different GP models. For the first model, we adopted only a QPC kernel, while the second model is represented by the combination of a QP kernel and a sinusoid. For the hyper-parameter representing the stellar rotation period, which is the same both in the QPC and QP GP kernels, we used the uninformative prior $\mathcal{U}(20,50)$ days. Both models are assumed to have an equal a-priori likelihood. As in our previous analyses we found that the QP plus planetary model is strongly favoured over the ‘GP-only’ QPC model ($\Delta \ln \mathcal{Z} = +7.3$, corresponding to an odds ratio of $\sim 1500:1$), following the convention usually adopted for model selection (e.g. Feroz et al. 2011, Table 1). This result shows that the ~ 18 day signal is much better fitted by a sinusoid rather than being modelled through a QPC kernel as the first harmonic of the stellar rotation period.

7. Discussion

From the best values of K_b and P_b derived in the previous section we derive a minimum mass for GJ 9689 b of $M_p \sin i = 9.65 \pm 1.41 M_\oplus$ and a semi-major axis $a = 0.1139 \pm 0.0039$ au (for the formulae see e.g. Cumming et al. 1999, Eqn. 1, 3). GJ 9689 b is therefore a super-Earth or a mini-Neptune like planet. Figure 17 shows the position of GJ 9689 b in the planetary mass vs. period diagram. For comparison purposes, the location of the known (radial velocity) planets around M dwarf stars are shown. It can be seen that GJ 9689 b has a period and a minimum mass similar to other HADES planets. Note that most of the HADES discoveries have periods shorter than 20 d and minimum masses lower than the mass of Neptune. Only one HADES planet, namely GJ 15 Ac, has a higher mass and an orbit at a wide distance from its host star, $P \sim 7600$ d (Pinamonti et al. 2018). This is in agreement with other radial velocity surveys that found that the frequency of gas-giant planets around M stars is lower than that around

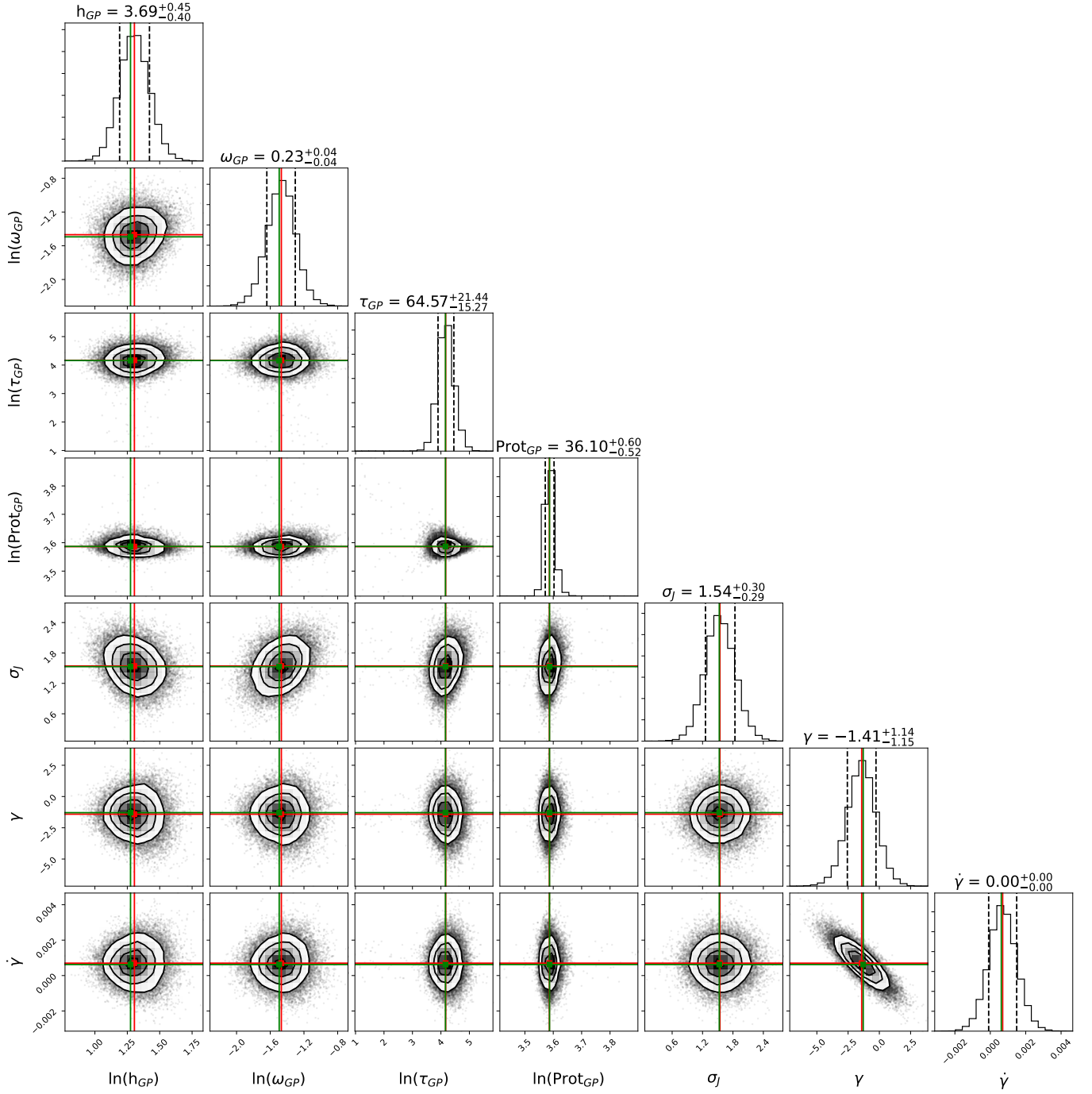


Fig. 13. Posterior distribution of the 'GP-only' model in which median and maximum a-posterior probability (MAP) have been marked (respectively, red and green line).

solar-type hosts (Endl et al. 2003, 2006; Butler et al. 2006; Bonfils et al. 2007; Cumming et al. 2008; Johnson et al. 2010).

Following the definition of Habitable Zone (HZ) of Kopparapu et al. (2013), the inner edge of the HZ for GJ 9689 was computed with the most optimistic limits (recent Venus) which corresponds to a semi-major axis of $a_{\text{HZ}} = 0.20$ au, which is larger than the orbit of GJ 9689 b. The equilibrium temperature of the planet can be determined from the balance between the incident

radiation from the host star, and that absorbed by the planet (or by its atmosphere). It can be written as:

$$T_{\text{eq}} = T_{\star} \left(\frac{R_{\star}}{2a} \right)^{1/2} [f(1 - A_B)]^{1/4} \quad (4)$$

where additional heat sources (such as the greenhouse effect) are not taken into account. In this equation A_B is the Bond albedo and f the heat redistribution factor. The value of f goes from $f = 1$ for an isotropic planetary emission, to $f = 2$ when only the day-side re-radiates the energy absorbed, as it could be the case for tidally-locked planets without oceans or atmosphere (Charbonneau et al. 2005; Méndez & Rivera-Valentín 2017). An upper

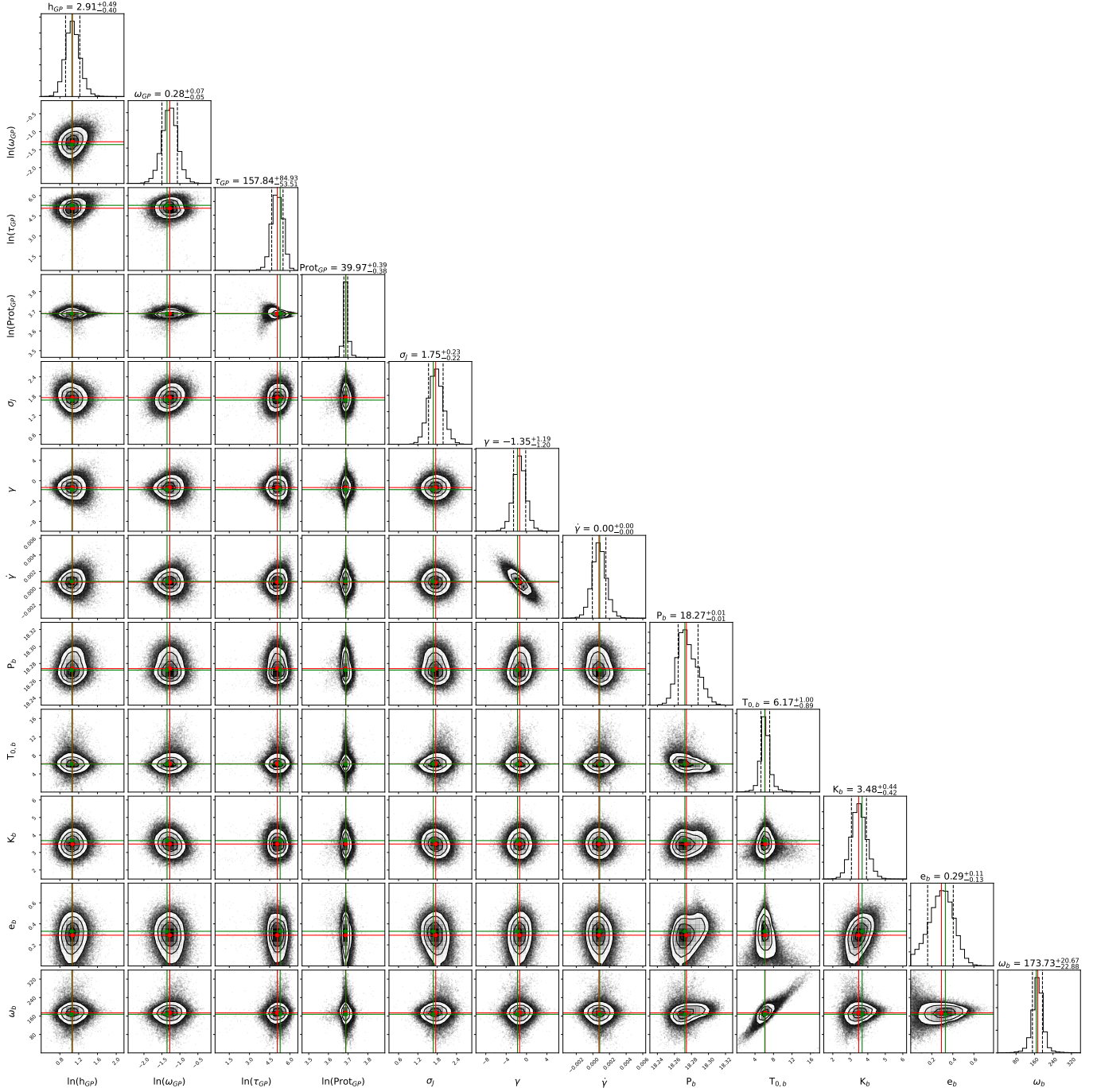


Fig. 14. Same as for Fig.13 but in the case of the 'Star-planet' model.

limit on T_{eq} may be obtained by setting $A_B = 0$. For GJ 9689 b we find upper limits on T_{eq} between 413.88 K ($f = 1$) and 492.19 K ($f = 2$). Therefore, GJ 9689 b have a T_{eq} which is ~ 140 -240 K higher than the equilibrium temperature of the rocky planets in our Solar System. For example Venus has $T_{eq} \sim 230$ K, while the Earth has a value of ~ 255 K, and for Mars we have $T_{eq} \sim 212$ K (Perryman 2018). However, the equilibrium temperature of GJ 9689 b is in agreement with the values derived for other super-Earth planets found around M dwarfs like GJ 3998 c, ~ 420 K, or Gl 886 b, ~ 379 -450 K (Affer et al. 2016, 2019).

The composition of exoplanets is an important but highly problematic issue. To start with, error uncertainties in stellar radius and mass are usually large and lower values of mass and

radius for the host star translate to overall higher densities (e.g. Modirrousta-Galian et al. 2020). Even if the planet transits, and accurate planetary mass and radius measurements are available, the composition of low-mass planets is plagued with degeneracies that arise mainly from trade-offs between the different composition building blocks (e.g. Valencia et al. 2007; Rogers & Seager 2010; Plotnykov & Valencia 2020).

In order to solve this problem, several works have suggested to use the abundances of refractory elements of the host star to constrain the refractory content of the planet, which is likely a good approximation from a statistical approach (e.g. Dorn et al. 2015; Brugger et al. 2017; Santos et al. 2017). Recently, Maldonado et al. (2020) determine the stellar abundances of a

Table 2. Best-fit values obtained for the 'Star-planet' model. Parameters e and ω are derived from the explored parameters $\sqrt{e} \cos(\omega)$ and $\sqrt{e} \sin(\omega)$.

Parameter	Prior	Description	Best-fit value
<i>Linear trend</i>			
γ (m s ⁻¹)	$\mathcal{U}(-10, 10)$	Ordinate	$-1.35^{+1.19}_{-1.20}$
$\dot{\gamma}$ (m s ⁻¹)	$\mathcal{U}(-10, 10)$	Slope	$0.00^{+0.00}_{-0.00}$
<i>GP parameters</i>			
σ_{Jit} (m s ⁻¹)	$\mathcal{U}(10^{-2}, 10^2)$	White noise term	$1.75^{+0.23}_{-0.22}$
h (m s ⁻¹)	$\mathcal{LU}(10^{-2}, 10^2)$	Amplitude of the covariance	$2.91^{+0.49}_{-0.40}$
τ (d)	$\mathcal{LU}(1, 10^5)$	Timescale of the exponential component	$157.84^{+84.93}_{-53.51}$
ω	$\mathcal{LU}(10^{-2}, 10)$	Weight of the periodic component	$0.28^{+0.07}_{-0.05}$
P_{rot} (d)	$\mathcal{LU}(30, 50)$	Rotation period	$39.97^{+0.39}_{-0.38}$
<i>Planet parameters</i>			
P_b (d)	$\mathcal{U}(15, 20)$	Period	$18.27^{+0.01}_{-0.01}$
$T_{0,b}$ (BJD-2,456,400 d)	$\mathcal{U}(0, 20)$	Time of periastron passage	$6.17^{+1.00}_{-0.89}$
K_b (m s ⁻¹)	$\mathcal{U}(0, 10)$	RV semi-amplitude	$3.48^{+0.44}_{-0.42}$
e_b	$\mathcal{U}(0, 0.8)$	Orbital eccentricity	$0.29^{+0.11}_{-0.13}, (< 0.34)$
ω_b (deg)	$\mathcal{U}(0, 360)$	Periastron angle	$173.73^{+20.67}_{-22.88}$
<i>Derived quantities</i>			
$M_b \sin i$ (M _⊕)		Minimum mass	9.65 ± 1.41
a_b (au)		Semi-major axis	0.1139 ± 0.0039
$T_{\text{eq},b}$ (K)		Equilibrium temperature	$413.88\text{--}492.19$

Table 3. Best-fit values obtained for the 'Star-planet' model when using the full dataset of RVs, and the data corresponding to the different seasons analysed in this work. The best-fit values obtained using the full RVs dataset and the QPC kernel are also given. Parameters e and ω are derived from the posterior distribution of $\sqrt{e} \cos(\omega)$ and $\sqrt{e} \sin(\omega)$.

Parameter	Full dataset	Season 1	Season 2	Season 3	Full dataset (QPC) kernel
P_b (d)	$18.27^{+0.01}_{-0.01}$	—	—	—	$18.27^{+0.01}_{-0.01}$
$T_{0,b}$ (d)	$6.17^{+1.00}_{-0.89}$	$6.25^{+5.63}_{-2.03}$	$7.61^{+2.00}_{-1.83}$	$7.69^{+2.80}_{-2.59}$	$6.19^{+1.05}_{-0.90}$
K_b (m/s)	$3.48^{+0.44}_{-0.42}$	$3.32^{+0.77}_{-0.75}$	$3.53^{+0.88}_{-0.74}$	$3.71^{+0.98}_{-0.92}$	$3.49^{+0.44}_{-0.43}$
e_b	$0.29^{+0.11}_{-0.13}$	$0.33^{+0.23}_{-0.21}$	$0.32^{+0.20}_{-0.20}$	$0.33^{+0.15}_{-0.17}$	$0.29^{+0.11}_{-0.13}$
ω_b (deg)	$173.73^{+20.67}_{-22.88}$	$167.67^{+48.90}_{-72.98}$	$178.17^{+37.16}_{-31.74}$	$177.19^{+49.47}_{-43.97}$	$173.47^{+20.80}_{-23.82}$

large sample of M dwarfs for several elements different from iron analysing high-resolution optical spectra. Using these abundances, we estimated the core mass fraction (CMF) of 52 rocky exoplanets (planetary masses between 1 and 20 M_⊕) around M dwarfs. We follow the CMF definition as provided in Schulze et al. (2020) that assumes that the planetary core is pure iron and the mantle reflects fully oxidised Mg and Si. The results are shown in Fig. 18 where the histogram of the derived CMFs is shown. We find that the CMF values of small planets around M dwarfs varies from 0.27 to 0.52 with a median value of 0.38. According to our results, GJ 9689 b have a CMF value 0.34, close to the median of the distribution. It is worth noticing that these values are slightly larger than the CMF values derived for 11 transiting planets around FGK stars (median CMF = 0.29) in Schulze et al. (2020). This trend, if confirmed, may indicate that small planets around M dwarfs might have larger cores.

Finally, we should note that the derived timescale of active regions is shorter in the 'GP-only' model than in the 'Star-planet'. While the former, $\tau_{\text{GP}} = 64.57^{+21.44}_{-15.27}$ d, is consistent with roughly two rotation periods, the latter, $\tau_{\text{GP}} = 157.84^{+84.93}_{-53.51}$ d, is much larger (around 4.0 rotation periods) and consistent with the typical active regions lifetimes derived for other M dwarf stars (Scandariato et al. 2017; Pinamonti et al. 2019). To fur-

ther investigate this issue, we run our 'GP-only' model for the S-index time series and the V band EXORAP photometry although the results do not allow us to reach a clear conclusion. Results for the S-index provide a typical active regions timescale of $\tau_{\text{GP}} = 63.87^{+79.64}_{-24.38}$ d, although the distribution is rather broad and has a tail towards larger values. However, the analysis of the V band photometry returns a correlation decay timescale of $\tau_{\text{GP}} = 38.27^{+41.91}_{-8.07}$ d which is comparable to the stellar rotation period, but a secondary peak appears at $\tau_{\text{GP}} \sim 100$ d. The corresponding corner plots can be seen in Fig. B.3 (S-index fit) and in Fig. B.4 (EXORAP photometry).

GJ 9689 is expected to be observed by the *Tess* mission (Ricker et al. 2015) in 2022, Sector 54 (July 9 to August 5, in cycle 4). In order to get an estimate of the transit probability and depth for GJ 9689 b, a value of the planetary radius is needed. Using the probabilistic mass–radius relationship by Chen & Kipping (2017), we obtain for GJ 9689 b a radius of $R_p = 2.92^{+1.05}_{-0.58} R_{\oplus}$ which implies a geometric transit probability of 2.5% and a transit depth of 0.23%. Although the transit probability is rather low, a potential transit might provide a constraining point in the mass-radius diagram of known planets and also enable determining the bulk density. A comparison of the CMF derived by assuming that the planet reflects the host star's major rocky build-

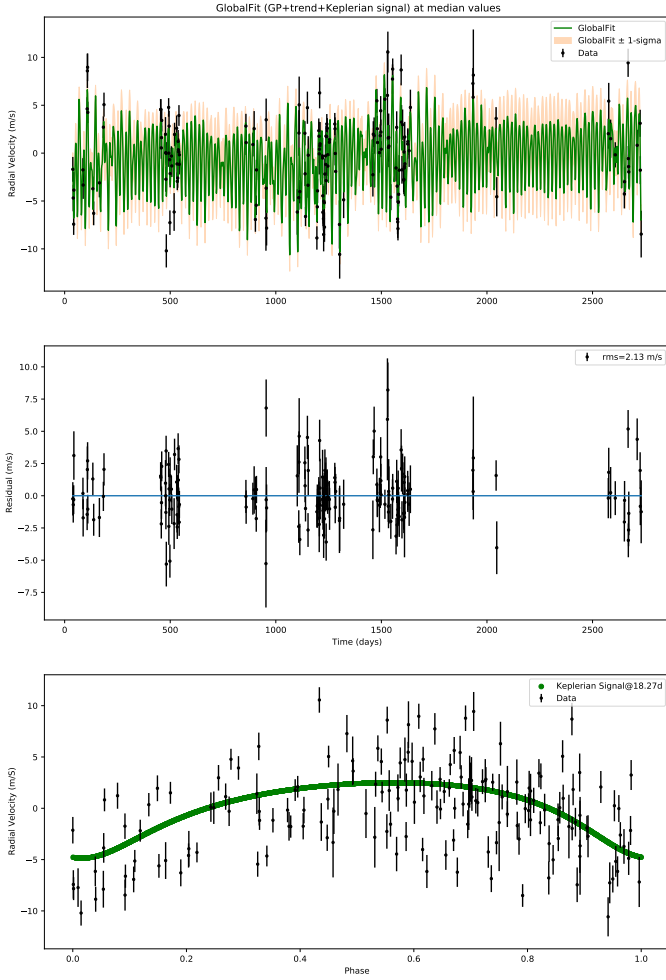


Fig. 15. Best-fit ‘Star-planet’ model (top), RV residuals (middle), and RV curve folded at the best-fit orbital period for GJ 9689 b (bottom).

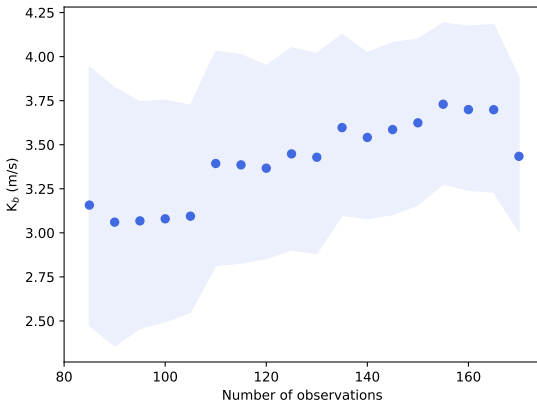


Fig. 16. RV semi-amplitude derived for GJ 9689 b using the ‘Star-planet’ model described in the text as a function of the number of observations. The shadow region indicates the 1σ uncertainties.

ing elemental abundances and the CMF value derived from the planetary bulk density might help us to unravel how GJ 9689 b formed and evolved.

Astrometric measurements are another source of information that might be used for the characterisation of the GJ 9689 planetary architecture. *Gaia* EDR3 data (Gaia Collaboration 2020)

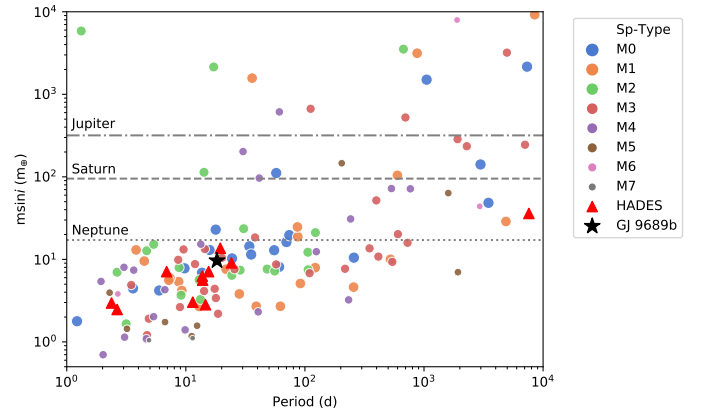


Fig. 17. Known radial velocity planets (planetary mass vs. orbital period diagram) around M dwarfs (As listed at <http://exoplanet.eu/> in December 2020). Planets discovered by the HADES survey are shown as red triangles. The planet GJ 9689 b is shown as a black star.

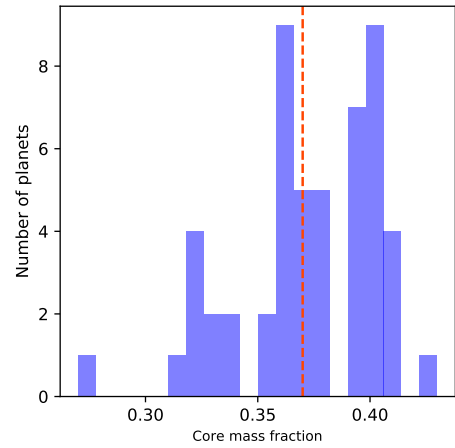


Fig. 18. Histogram of derived CMF for suspected rocky planets around M dwarfs. The vertical red line shows the median of the distribution.

shows that GJ 9689 has an astrometric noise of $73\mu\text{as}$ (with a statistical significance of 6.5σ) and a Renormalised Unit Weight Error (RUWE) value of 0.996. Furthermore, no significant proper motion anomaly between *Gaia* DR2 and *Hipparcos* has been reported (Kervella et al. 2019). Therefore, it is plausible that there are no massive companions at long periods. Detailed RV detection limits for the stars observed within the framework of the HADES survey will be addressed in a forthcoming work.

It is worth noticing that GJ 9689 b is not the first planet around an M dwarf with an orbital period close to half the stellar rotation period. Some examples include Gl 49 b (Perger et al. 2019) or GJ 720 Ab (González-Álvarez et al. 2021). The detection of such planets is challenging. It is known that dark spots in the stellar surface might produce a RV modulation with a period of $P_{\text{rot}}/2$, while the induced RV period due to the suppression of the surface convection is equal to P_{rot} (see e.g. Lanza et al. 2010). The period found in the RV might be slightly different from $P_{\text{rot}}/2$ due to several phenomena such as differential rotation or the evolution of the spot in the active longitude. While lifetimes of active longitudes are not well known, the possibility of an active longitude with time scales of several years might not be excluded in M dwarfs. Note that single spots may survive even for hundreds of days in the surface of M dwarfs (e.g. Giles et al. 2017). In the case of GJ 9689, given its rotational period

and the photometric variability of the star, and assuming a stable active longitude covered by dark spots with an area of 1% of the stellar disc, we derive a semi-amplitude of $\sim 7.2 \text{ ms}^{-1}$ for the signal due to the magnetic activity of such spots (which is larger than the observed RV variability).

This consideration and all the analysis performed in this work make us confident that the signal at 18.27 d found in the RV time-series of GJ 9689 is truly Keplerian in nature. An 'ultimate' confirmation of planets like GJ 9689 b will likely be possible in a near future if high-resolution spectrographs in the near infrared domain are able to reach enough RV precision.

8. Conclusions

Understanding the origin and evolution of stars and planetary systems is one of the major goals in modern Astrophysics. M dwarfs have emerged as promising targets in the search for small planets. Being less massive and cooler than solar-type stars, planets have a larger radial velocity amplitude and their habitable zones are closer to the host star (e.g. Reiners et al. 2010). However, the expected periods of planets in the habitable zone around M stars may be comparable to the rotation period of the host star. As a consequence, unravelling the origin (stellar or truly Keplerian) of periodic signals in the RV dataset of M dwarfs is a complicated task.

The nearby M dwarf GJ 9689 is an example of this problematic. In this work we have analysed more than seven years of RV data points of GJ 9689. The radial velocity analysis reveals two signals at 39.31 d and 18.21 d. A detailed study of the main activity indexes and photometry allows us to identify the 39.31 d as the rotation period of the star. This hypothesis is confirmed by studying the stability of this signal as a function of the number of observations, epoch of observations, and spectral range used to compute the radial velocity.

A careful analysis of the spectral window in several observing seasons shows that the 18.27 d signal is not an harmonic or an alias of the 39.32 d period. In addition, activity indexes, CCF asymmetry indicators, and photometric data show no variability at all at 18.27 d. The signal is stable in all analysed epochs, it does not show variations with the number of observations, and it is also visible even if only the reddest part of the spectra are used in the computation of the radial velocity dataset. We therefore conclude that the 18.27 d signal is most likely truly Keplerian in nature. In order to derive the minimum mass and orbital parameters of GJ 9689 b we fitted the RV time series with a Keplerian model combined with a GP quasi-periodic model to take into account the stellar activity signal. We obtain a period $P = 18.27 \pm 0.01$ d, a semi-major axis of $a = 0.114 \pm 0.004$ au, and a minimum mass of $M_p \sin i = 9.65 \pm 1.41 M_\oplus$. Assuming that the composition of a rocky planet directly mirrors the relative Fe, Mg, and Si abundances of its host we derived the CMF of several suspected rocky planets around M dwarfs, finding that the CMF value of GJ 9689 b is close to the median value of the distribution.

GJ 9689 b joins the population of Super-Earths at short periods ($P < 20$ d) around M dwarfs that is currently emerging (see Fig. 17). Further studies of the properties of these planets will help us to explore a regime of protoplanetary disc and host stars conditions very different from FGK stars, providing additional constraints for planet formation models.

Acknowledgements. J.M., and G.M. acknowledge support from the accordo attuativo ASI-INAF n.2021-5-HH.0 "Partecipazione italiana alla fase B2/C della missione Ariel". A.P., A.M., M.P., and A.S. acknowledge partial contribution from the agreement ASI-INAF n.2018-16-HH.0. E.G.A. acknowl-

edge support from the Spanish Ministry for Science, Innovation, and Universities through projects AYA-2016-79425-C3-1/2/3-P, AYA2015-69350-C3-2-P, ESP2017-87676-C5-2-R, ESP2017-87143-R. The Centro de Astrobiología (CAB, CSIC-INTA) is a Center of Excellence "Maria de Maeztu". M.P. and I.R. acknowledge support from the Spanish Ministry of Science and Innovation and the European Regional Development Fund through grant PGC2018-098153-B-C33, as well as the support of the Generalitat de Catalunya/CERCA programme. J.I.G.H. acknowledges financial support from Spanish Ministry of Science and Innovation (MICINN) under the 2013 Ramón y Cajal program RYC-2013-14875. B.T.P. acknowledges Fundación La Caixa for the financial support received in the form of a Ph.D. contract. A.S.M. acknowledges financial support from the Spanish MICINN under the 2019 Juan de la Cierva Programme. B.T.P., A.S.M., J.I.G.H., R.R. acknowledge financial support from the Spanish MICINN AYA2017-86389-P. This work has made use of data from the European Space Agency (ESA) mission *Gaia* (<https://www.cosmos.esa.int/gaia>), processed by the *Gaia* Data Processing and Analysis Consortium (DPAC, <https://www.cosmos.esa.int/web/gaia/dpac/consortium>). Funding for the DPAC has been provided by national institutions, in particular the institutions participating in the *Gaia* Multilateral Agreement.

References

- Affer, L., Damasso, M., Micela, G., et al. 2019, *A&A*, 622, A193
 Affer, L., Micela, G., Damasso, M., et al. 2016, *A&A*, 593, A117
 Ambikasaran, S., Foreman-Mackey, D., Greengard, L., Hogg, D. W., & O'Neil, M. 2014
 Anglada-Escudé, G. & Butler, R. P. 2012, *ApJS*, 200, 15
 Baranne, A., Queloz, D., Mayor, M., et al. 1996, *A&AS*, 119, 373
 Bensby, T., Feltzing, S., & Lundström, I. 2003, *A&A*, 410, 527
 Bensby, T., Feltzing, S., Lundström, I., & Ilyin, I. 2005, *A&A*, 433, 185
 Boisse, I., Moutou, C., Vidal-Madjar, A., et al. 2009, *A&A*, 495, 959
 Bonfils, X., Delfosse, X., Udry, S., et al. 2013, *A&A*, 549, A109
 Bonfils, X., Mayor, M., Delfosse, X., et al. 2007, *A&A*, 474, 293
 Brügger, B., Mousis, O., Deleuil, M., & Deschamps, F. 2017, *ApJ*, 850, 93
 Buchner, J., Georgakakos, A., Nandra, K., et al. 2014, *A&A*, 564, A125
 Butler, R. P., Johnson, J. A., Marcy, G. W., et al. 2006, *PASP*, 118, 1685
 Chabrier, G. & Baraffe, I. 2000, *ARA&A*, 38, 337
 Charbonneau, D., Allen, L. E., Megeath, S. T., et al. 2005, *ApJ*, 626, 523
 Chen, J. & Kipping, D. 2017, *ApJ*, 834, 17
 Courcol, B., Bouchy, F., & Deleuil, M. 2016, *MNRAS*, 461, 1841
 Cumming, A. 2010, *Statistical Distribution of Exoplanets*, ed. S. Seager, 191–214
 Cumming, A., Butler, R. P., Marcy, G. W., et al. 2008, *PASP*, 120, 531
 Cumming, A., Marcy, G. W., & Butler, R. P. 1999, *ApJ*, 526, 890
 Curran, P. A. 2014, *arXiv e-prints*, arXiv:1411.3816
 Cutri, R. M., Skrutskie, M. F., van Dyk, S., et al. 2003, *VizieR Online Data Catalog*, 2246
 Desort, M., Lagrange, A.-M., Galland, F., Udry, S., & Mayor, M. 2007, *A&A*, 473, 983
 Dorn, C., Khan, A., Heng, K., et al. 2015, *A&A*, 577, A83
 Dressing, C. D. & Charbonneau, D. 2013, *ApJ*, 767, 95
 Dressing, C. D. & Charbonneau, D. 2015, *ApJ*, 807, 45
 Dumusque, X., Borsari, F., Damasso, M., et al. 2017, *A&A*, 598, A133
 Dumusque, X., Santos, N. C., Udry, S., Lovis, C., & Bonfils, X. 2011a, *A&A*, 527, A82
 Dumusque, X., Udry, S., Lovis, C., Santos, N. C., & Monteiro, M. J. P. F. G. 2011b, *A&A*, 525, A140
 Edelson, R. A. & Krolik, J. H. 1988, *ApJ*, 333, 646
 Endl, M., Cochran, W. D., Kürster, M., et al. 2006, *ApJ*, 649, 436
 Endl, M., Cochran, W. D., Tull, R. G., & MacQueen, P. J. 2003, *AJ*, 126, 3099
 Endl, M., Kürster, M., Els, S., Hatzes, A. P., & Cochran, W. D. 2001, *A&A*, 374, 675
 ESA, ed. 1997, *ESA Special Publication*, Vol. 1200, *The HIPPARCOS and TYCHO catalogues. Astrometric and photometric star catalogues derived from the ESA HIPPARCOS Space Astrometry Mission*
 Feliz, D. L., Plavchan, P., Bianco, S. N., et al. 2021, *AJ*, 161, 247
 Feroz, F., Balan, S. T., & Hobson, M. P. 2011, *Monthly Notices of the Royal Astronomical Society*, 415, 3462
 Feroz, F., Hobson, M. P., Cameron, E., & Pettitt, A. N. 2019, *The Open Journal of Astrophysics*, 2, 10
 Foreman-Mackey, D., Hogg, D. W., Lang, D., & Goodman, J. 2013, *PASP*, 125, 306
 Fulton, B. J., Petigura, E. A., Blunt, S., & Sinukoff, E. 2018, *PASP*, 130, 044504
 Gaia Collaboration. 2020, *VizieR Online Data Catalog*, I/350
 Giles, H. A. C., Collier Cameron, A., & Haywood, R. D. 2017, *MNRAS*, 472, 1618
 Gillon, M., Triaud, A. H. M. J., Fortney, J. J., et al. 2012, *A&A*, 542, A4

- Gomes da Silva, J., Figueira, P., Santos, N., & Faria, J. 2018, *The Journal of Open Source Software*, 3, 667
- Gomes da Silva, J., Santos, N. C., Bonfils, X., et al. 2011, *A&A*, 534, A30
- González-Álvarez, E., Micela, G., Maldonado, J., et al. 2019, *A&A*, 624, A27
- González-Álvarez, E., Petralia, A., Micela, G., et al. 2021, *arXiv e-prints*, arXiv:2103.09643
- Goodman, J. & Weare, J. 2010, *Commun. Appl. Math. Comput. Sci.*, 5, 65
- Hobson, M. J., Delfosse, X., Astudillo-Defru, N., et al. 2019, *A&A*, 625, A18
- Howard, A. W. 2013, *Science*, 340, 572
- Howard, A. W., Marcy, G. W., Bryson, S. T., et al. 2012, *ApJS*, 201, 15
- Johnson, J. A. & Apps, K. 2009, *ApJ*, 699, 933
- Johnson, J. A., Howard, A. W., Marcy, G. W., et al. 2010, *PASP*, 122, 149
- Kass, R. E. & Raftery, A. E. 1995, *Journal of the American Statistical Association*, 90, 773
- Kervella, P., Arenou, F., Mignard, F., & Thévenin, F. 2019, *A&A*, 623, A72
- Klein, B., Donati, J.-F., Moutou, C., et al. 2021, *MNRAS*, 502, 188
- Kopparapu, R. K., Ramirez, R., Kasting, J. F., et al. 2013, *ApJ*, 765, 131
- Lanza, A. F., Bonomo, A. S., Moutou, C., et al. 2010, *A&A*, 520, A53
- Lovis, C. & Pepe, F. 2007, *A&A*, 468, 1115
- Maldonado, J., Affer, L., Micela, G., et al. 2015, *A&A*, 577, A132
- Maldonado, J., Martínez-Arnáiz, R. M., Eiroa, C., Montes, D., & Montesinos, B. 2010, *A&A*, 521, A12
- Maldonado, J., Micela, G., Baratella, M., et al. 2020, *A&A*, 644, A68
- Maldonado, J., Scandariato, G., Stelzer, B., et al. 2017, *A&A*, 598, A27
- Mann, A. W., Gaidos, E., Lépine, S., & Hilton, E. J. 2012, *ApJ*, 753, 90
- Mayor, M. & Queloz, D. 1995, *Nature*, 378, 355
- Méndez, A. & Rivera-Valentín, E. G. 2017, *ApJ*, 837, L1
- Modirrousta-Galian, D., Stelzer, B., Magaúda, E., et al. 2020, *A&A*, 641, A113
- Montes, D., López-Santiago, J., Gálvez, M. C., et al. 2001, *MNRAS*, 328, 45
- Montet, B. T., Crepp, J. R., Johnson, J. A., Howard, A. W., & Marcy, G. W. 2014, *ApJ*, 781, 28
- Mortier, A. & Collier Cameron, A. 2017, *A&A*, 601, A110
- Mortier, A., Faria, J. P., Correia, C. M., Santerne, A., & Santos, N. C. 2015, *A&A*, 573, A101
- Neves, V., Bonfils, X., Santos, N. C., et al. 2013, *A&A*, 551, A36
- Nutzman, P. & Charbonneau, D. 2008, *PASP*, 120, 317
- Paulson, D. B., Cochran, W. D., & Hatzes, A. P. 2004, *AJ*, 127, 3579
- Pepe, F., Cristiani, S., Rebolo, R., et al. 2021, *A&A*, 645, A96
- Pepe, F., Mayor, M., Galland, F., et al. 2002, *A&A*, 388, 632
- Perger, M., Anglada-Escudé, G., Ribas, I., et al. 2021, *A&A*, 645, A58
- Perger, M., García-Piquer, A., Ribas, I., et al. 2017a, *A&A*, 598, A26
- Perger, M., Ribas, I., Damasso, M., et al. 2017b, *A&A*, 608, A63
- Perger, M., Scandariato, G., Ribas, I., et al. 2019, *A&A*, 624, A123
- Perryman, M. 2018, *The Exoplanet Handbook*
- Pinamonti, M., Damasso, M., Marzari, F., et al. 2018, *A&A*, 617, A104
- Pinamonti, M., Sozzetti, A., Giacobbe, P., et al. 2019, *A&A*, 625, A126
- Plotnikov, M. & Valencia, D. 2020, *MNRAS*, 499, 932
- Queloz, D., Bouchy, F., Moutou, C., et al. 2009, *A&A*, 506, 303
- Queloz, D., Henry, G. W., Sivan, J. P., et al. 2001, *A&A*, 379, 279
- Radick, R. R., Lockwood, G. W., Henry, G. W., Hall, J. C., & Pevtsov, A. A. 2018, *ApJ*, 855, 75
- Rainer, M., Borsa, F., & Affer, L. 2020, *Experimental Astronomy*, 49, 73
- Reiners, A., Bean, J. L., Huber, K. F., et al. 2010, *ApJ*, 710, 432
- Ricker, G. R., Winn, J. N., Vanderspek, R., et al. 2015, *Journal of Astronomical Telescopes, Instruments, and Systems*, 1, 014003
- Robertson, D. R. S., Gallo, L. C., Zoghbi, A., & Fabian, A. C. 2015, *MNRAS*, 453, 3455
- Rogers, L. A. & Seager, S. 2010, *ApJ*, 712, 974
- Rojas-Ayala, B., Covey, K. R., Muirhead, P. S., & Lloyd, J. P. 2012, *ApJ*, 748, 93
- Saar, S. H. & Donahue, R. A. 1997, *ApJ*, 485, 319
- Santos, N. C., Adibekyan, V., Dorn, C., et al. 2017, *A&A*, 608, A94
- Santos, N. C., Mayor, M., Naef, D., et al. 2000, *A&A*, 361, 265
- Scandariato, G., Maldonado, J., Affer, L., et al. 2017, *A&A*, 598, A28
- Schlaufman, K. C. & Laughlin, G. 2010, *A&A*, 519, A105
- Schneider, J., Dedieu, C., Le Sidaner, P., Savalle, R., & Zolotukhin, I. 2011, *A&A*, 532, A79
- Schulze, J. G., Wang, J., Johnson, J. A., Unterborn, C. T., & Panero, W. R. 2020, *arXiv e-prints*, arXiv:2011.08893
- Sokal, A. 1996
- Sozzetti, A., Bernagozzi, A., Bertolini, E., et al. 2013, in *European Physical Journal Web of Conferences*, Vol. 47, *European Physical Journal Web of Conferences*, 03006
- Suárez Mascareño, A., González Hernández, J. I., Rebolo, R., et al. 2017, *A&A*, 605, A92
- Suárez Mascareño, A., Rebolo, R., González Hernández, J. I., et al. 2018, *A&A*, 612, A89
- Terrien, R. C., Mahadevan, S., Bender, C. F., et al. 2012, *ApJ*, 747, L38
- Toledo-Padrón, B., Suárez Mascareño, A., González Hernández, J. I., et al. 2021, *A&A*, 648, A20
- Tuomi, M., Anglada-Escudé, G., Gerlach, E., et al. 2013, *A&A*, 549, A48
- Tuomi, M., Jones, H. R. A., Barnes, J. R., Anglada-Escudé, G., & Jenkins, J. S. 2014, *MNRAS*, 441, 1545
- Udry, S. & Santos, N. C. 2007, *ARA&A*, 45, 397
- Valencia, D., Sasselov, D. D., & O'Connell, R. J. 2007, *ApJ*, 656, 545
- Wolszczan, A. & Frail, D. A. 1992, *Nature*, 355, 145
- Wright, J. T. 2005, *PASP*, 117, 657
- Wright, J. T., Mahadevan, S., Hearty, F., et al. 2018, in *American Astronomical Society Meeting Abstracts*, Vol. 231, *American Astronomical Society Meeting Abstracts #231*, 246.45
- Zechmeister, M., Dreizler, S., Ribas, I., et al. 2019, *A&A*, 627, A49
- Zechmeister, M. & Kürster, M. 2009, *A&A*, 496, 577

Appendix A: Additional tables

Table A.1 provides the observational data collected with the HARPS-N spectrograph for GJ 9689 and used in the present study. We list the observations dates (in barycentric Julian date or BJD), the RVs, and activity S, $H\alpha$, and Na I D₁, D₂ indexes with their corresponding uncertainties.

Appendix B: Online figures

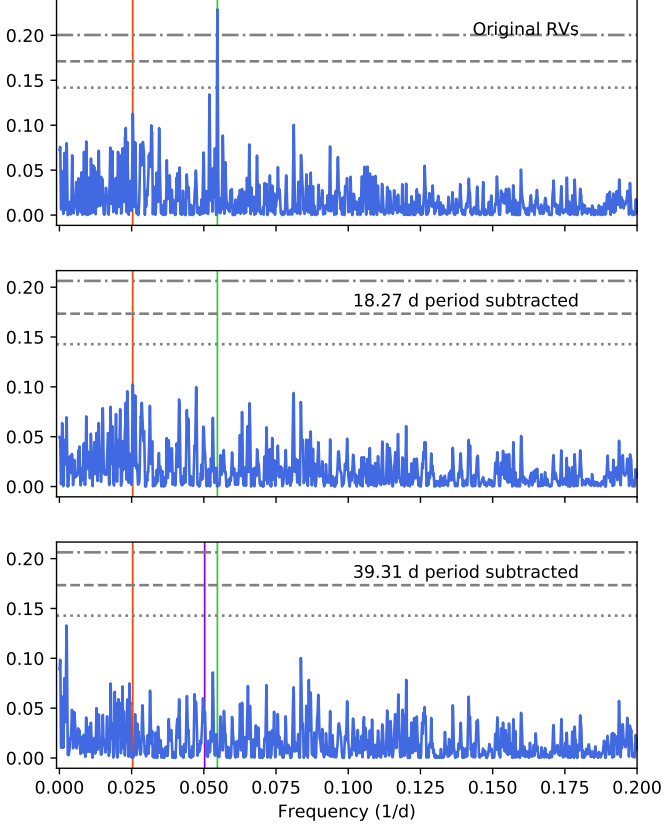


Fig. B.1. Top: GLS periodogram of the DRS RV measurements. Middle: GLS periodogram after subtracting the 18.27 d period. Bottom: GLS periodogram after subtracting the 18.27 and the 39.31 d signals. Values corresponding to a FAP of 10%, 1%, and 0.1% are shown with horizontal grey lines. The vertical red line indicates the period at 39.31 d while the vertical green line shows the 18.27 d period. The first harmonic of the 39.31 d signal is shown in violet.

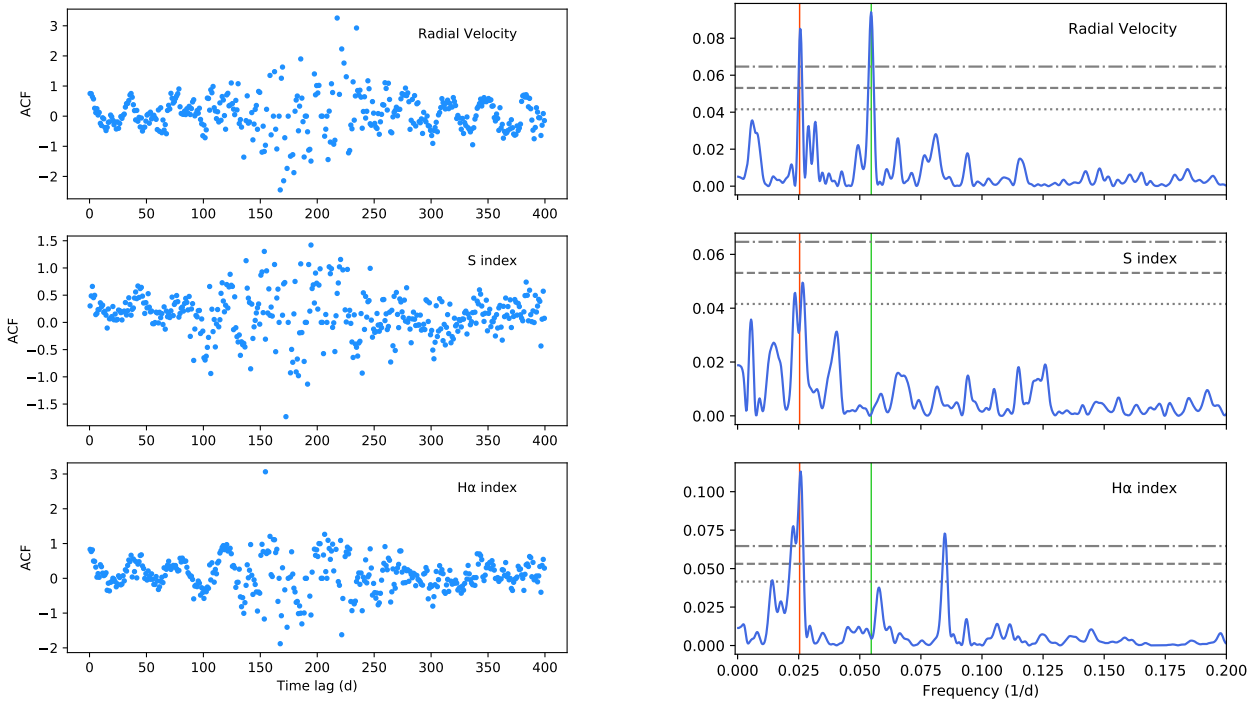


Fig. B.2. Left: autocorrelation function of RV, S-index, and H α time-series. Right: Corresponding GLS diagrams.

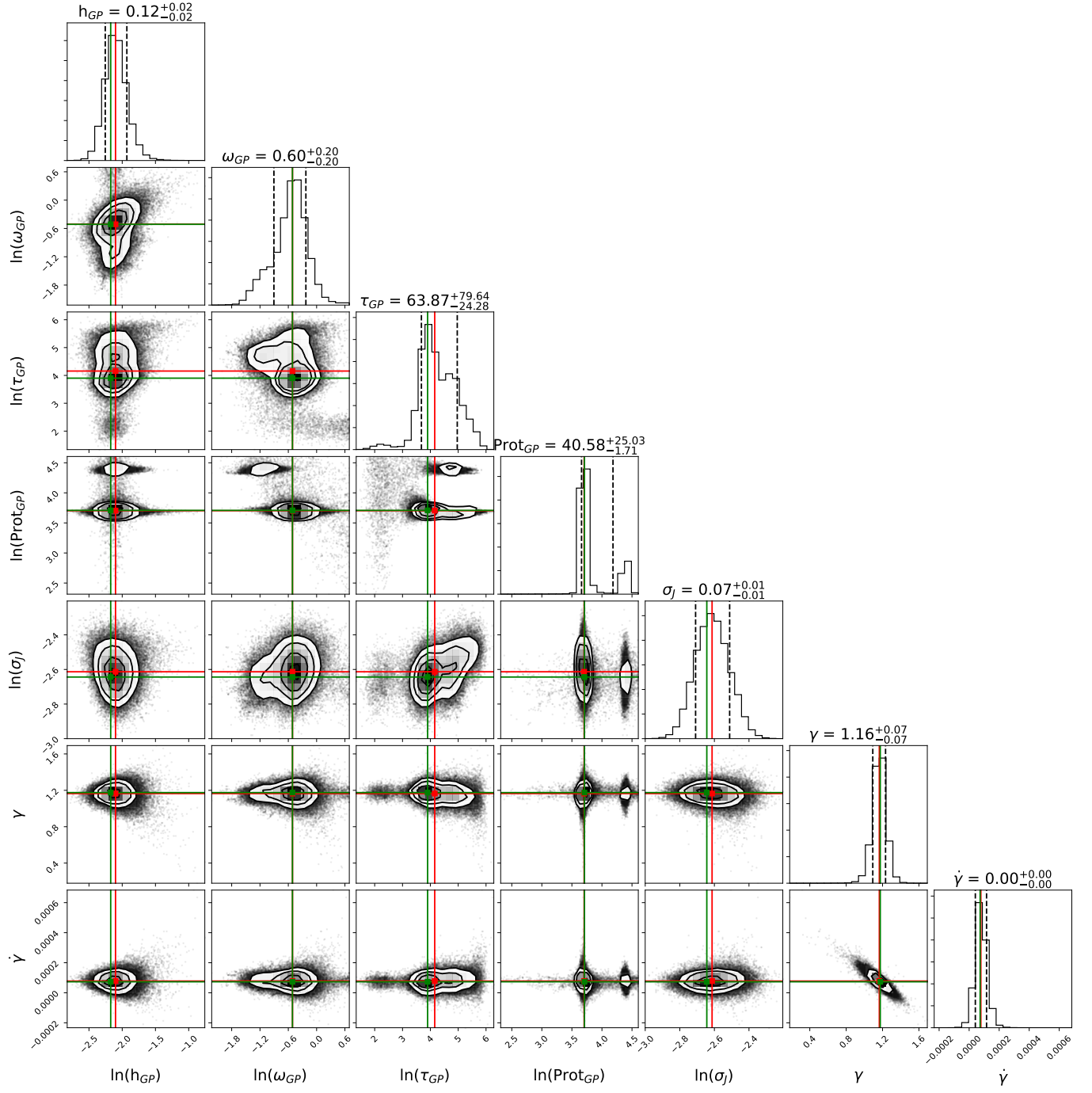


Fig. B.3. Posterior distribution of the 'GP-only' model of the S-index time series in which median and maximum a-posterior probability (MAP) have been marked (respectively, red and green line).

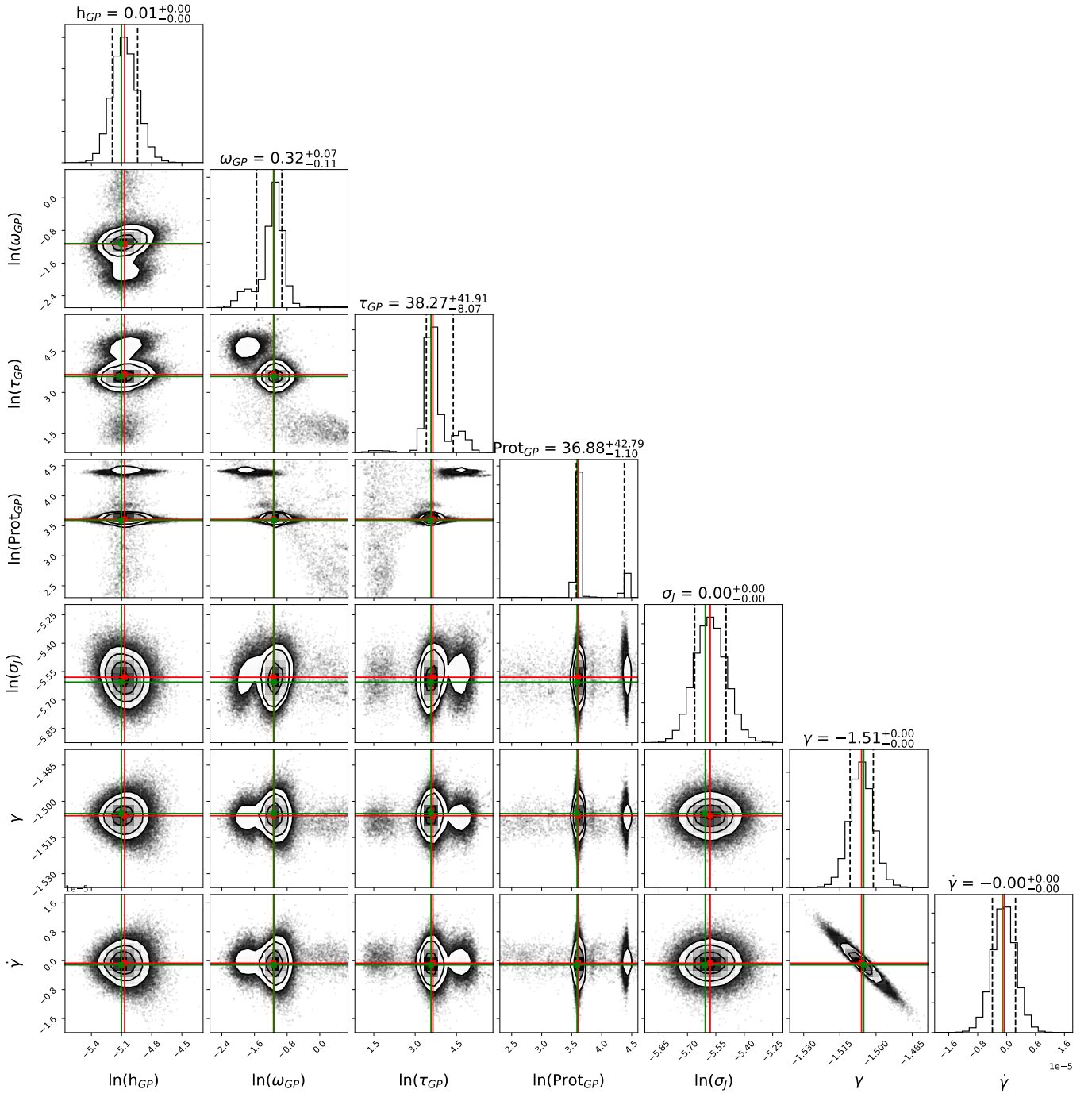


Fig. B.4. Posterior distribution of the 'GP-only' model of the EXORAP V band photometry in which median and maximum a-posterior probability (MAP) have been marked (respectively, red and green line).

Table A.1. Observation log of GJ 9689

BJD - 2400000 (d)	RV (ms ⁻¹)	Δ RV (ms ⁻¹)	S-index	Δ (S-index)	H α -index	Δ (H α -index)	Na I-index	Δ (Na I-index)
56438.684901	-1.69	1.29	1.1905	0.0098	0.3444	0.0008	0.1274	0.0008
56440.698234	-4.69	1.39	1.0702	0.0127	0.3420	0.0009	0.1212	0.0010
56442.687720	-7.42	1.12	1.0101	0.0093	0.3381	0.0008	0.1219	0.0008
56443.663855	-3.86	1.88	0.9711	0.0211	0.3369	0.0013	0.1234	0.0015
56486.620666	-1.75	1.22	1.1106	0.0133	0.3395	0.0010	0.1219	0.0010
56487.580888	-3.33	1.45	1.1052	0.0142	0.3388	0.0010	0.1198	0.0010
56506.483363	4.62	1.22	1.1593	0.0115	0.3400	0.0009	0.1250	0.0009
56507.593975	8.59	1.79	1.3207	0.0182	0.3484	0.0009	0.1226	0.0011
56508.608809	8.97	1.45	1.2414	0.0127	0.3397	0.0008	0.1237	0.0009
56509.619800	4.26	1.11	1.3287	0.0138	0.3498	0.0009	0.1274	0.0010
56533.476873	-3.72	1.27	0.9790	0.0099	0.3389	0.0008	0.1201	0.0008
56537.502695	-6.29	1.24	1.0663	0.0093	0.3391	0.0007	0.1179	0.0007
56564.543673	-3.11	1.51	1.2143	0.0157	0.3414	0.0010	0.1237	0.0011
56583.391762	2.71	1.13	1.0735	0.0104	0.3399	0.0008	0.1220	0.0008
56586.321128	5.07	1.25	1.2484	0.0128	0.3459	0.0007	0.1230	0.0009
56854.577773	4.55	1.08	1.2765	0.0102	0.3419	0.0007	0.1283	0.0008
56855.567308	4.57	1.07	1.2634	0.0104	0.3467	0.0008	0.1292	0.0008
56857.677235	0.55	1.14	1.2984	0.0116	0.3482	0.0007	0.1262	0.0008
56858.630655	1.62	1.26	1.2757	0.0130	0.3448	0.0008	0.1266	0.0009
56859.643762	3.42	1.16	1.2015	0.0147	0.3453	0.0008	0.1239	0.0009
56877.602491	1.97	1.79	1.2235	0.0243	0.3424	0.0012	0.1282	0.0015
56878.585884	0.05	1.07	1.1074	0.0097	0.3417	0.0008	0.1246	0.0008
56879.494416	-2.73	1.31	1.1120	0.0119	0.3426	0.0010	0.1236	0.0010
56880.485352	-0.03	1.18	1.0715	0.0109	0.3467	0.0009	0.1260	0.0009
56881.470848	-10.21	1.73	1.2427	0.0200	0.3501	0.0013	0.1282	0.0013
56892.466346	4.78	0.97	1.2800	0.0093	0.3464	0.0007	0.1257	0.0007
56893.481535	0.00	1.43	1.3666	0.0176	0.3471	0.0011	0.1264	0.0012
56894.484073	2.82	1.58	1.3408	0.0151	0.3501	0.0010	0.1268	0.0011
56897.506643	-0.69	1.24	1.3410	0.0157	0.3478	0.0012	0.1274	0.0011
56898.464617	-7.26	1.28	1.2680	0.0138	0.3480	0.0010	0.1266	0.0010
56899.477380	-2.14	1.44	1.3657	0.0173	0.3507	0.0012	0.1250	0.0012
56905.470066	-0.30	1.02	1.2288	0.0109	0.3431	0.0008	0.1259	0.0008
56907.464509	-1.34	1.15	1.1404	0.0104	0.3410	0.0008	0.1233	0.0008
56918.472879	-6.15	1.97	1.1111	0.0237	0.3420	0.0014	0.1319	0.0016
56920.469597	1.95	1.23	1.1492	0.0128	0.3441	0.0009	0.1233	0.0010
56928.458456	14.93	3.72	1.0998	0.0441	0.3423	0.0012	0.1202	0.0021
56930.505522	2.59	1.34	1.1514	0.0126	0.3390	0.0008	0.1236	0.0009
56932.461632	-1.13	1.38	1.1538	0.0189	0.3406	0.0012	0.1239	0.0013
56933.355305	-2.94	0.93	1.2501	0.0117	0.3435	0.0008	0.1256	0.0008
56935.349440	-2.61	1.01	1.3033	0.0097	0.3440	0.0007	0.1270	0.0007
56937.459316	1.23	1.19	1.2586	0.0113	0.3444	0.0008	0.1282	0.0008
56938.464540	0.35	1.18	1.2257	0.0108	0.3477	0.0007	0.1293	0.0008
56940.460277	0.11	1.40	1.3123	0.0120	0.3471	0.0009	0.1292	0.0009
56941.347152	3.93	1.08	1.1803	0.0087	0.3448	0.0007	0.1277	0.0007
56942.454785	-1.17	1.06	1.2207	0.0110	0.3438	0.0007	0.1246	0.0008
56943.451164	-0.18	1.06	1.2204	0.0109	0.3462	0.0007	0.1243	0.0008
57258.456713	2.82	1.28	1.2957	0.0127	0.3509	0.0008	0.1283	0.0009
57259.479424	1.10	1.30	1.5259	0.0171	0.3656	0.0010	0.1341	0.0011
57291.395613	0.90	1.24	1.3580	0.0123	0.3555	0.0009	0.1310	0.0009
57297.467722	2.55	1.84	1.2680	0.0220	0.3441	0.0010	0.1198	0.0013
57303.423054	-6.93	1.28	1.1434	0.0112	0.3463	0.0008	0.1276	0.0009
57307.409630	-5.44	1.02	1.0423	0.0098	0.3371	0.0009	0.1230	0.0008
57308.417641	-1.76	1.06	1.1055	0.0093	0.3370	0.0008	0.1225	0.0008
57352.336645			0.5182	0.2654	0.3394	0.0109	0.1491	0.0310
57353.310991	-6.79	3.41	1.3845	0.0587	0.3437	0.0022	0.1221	0.0032
57354.304734	3.48	2.22	1.2338	0.0448	0.3410	0.0019	0.1252	0.0025
57354.317418	-3.66	2.54	1.0779	0.0421	0.3435	0.0020	0.1287	0.0026
57356.308205	-7.83	1.82	1.1784	0.0203	0.3392	0.0012	0.1230	0.0013
57501.700690	-6.15	2.37	1.3670	0.0415	0.3617	0.0018	0.1388	0.0024
57508.699547	-4.65	1.26	1.3434	0.0178	0.3489	0.0008	0.1259	0.0011

Table A.1. Continued.

BJD - 2400000 (d)	RV (ms ⁻¹)	Δ RV (ms ⁻¹)	S-index	Δ (S-index)	H α -index	Δ (H α -index)	Na I-index	Δ (Na I-index)
57509.691609	2.10	2.39	1.1425	0.0303	0.3446	0.0012	0.1248	0.0017
57510.683844	5.04	2.95	1.2858	0.0266	0.3399	0.0010	0.1210	0.0014
57513.706098	-4.02	1.22	1.1946	0.0128	0.3430	0.0008	0.1238	0.0009
57537.707450	2.07	1.26	1.5314	0.0138	0.3650	0.0009	0.1350	0.0010
57538.662184	-2.16	1.28	1.6772	0.0159	0.3841	0.0008	0.1372	0.0010
57540.697701	-6.62	1.00	1.5303	0.0131	0.3708	0.0007	0.1328	0.0008
57549.682126	4.74	1.68	1.3937	0.0170	0.3498	0.0007	0.1220	0.0010
57552.625769	-3.35	1.31	1.2904	0.0137	0.3494	0.0009	0.1277	0.0010
57553.657209	-0.22	1.99	1.2436	0.0204	0.3455	0.0012	0.1438	0.0015
57594.557626	-8.86	1.22	1.3356	0.0137	0.3453	0.0008	0.1273	0.0009
57596.591265	-5.61	1.68	1.2850	0.0221	0.3466	0.0012	0.1268	0.0014
57597.552753	-3.94	1.27	1.3464	0.0161	0.3459	0.0009	0.1219	0.0010
57603.557020	2.35	1.28	1.3456	0.0132	0.3474	0.0008	0.1274	0.0009
57604.544702	1.77	1.50	1.2943	0.0167	0.3497	0.0010	0.1246	0.0012
57605.641977	-0.07	2.15	1.3678	0.0295	0.3528	0.0012	0.1246	0.0017
57606.550501	0.41	1.42	1.3565	0.0183	0.3519	0.0010	0.1294	0.0012
57607.570725	6.29	1.61	1.4251	0.0218	0.3557	0.0010	0.1252	0.0013
57608.638735	0.77	1.01	1.4773	0.0180	0.3574	0.0009	0.1293	0.0011
57609.585843	0.97	2.28	1.3597	0.0389	0.3549	0.0016	0.1320	0.0022
57620.487606	-0.29	1.83	1.6431	0.0236	0.3570	0.0013	0.1356	0.0015
57621.519280	-0.51	2.12	1.2062	0.0324	0.3524	0.0015	0.1353	0.0021
57622.503754	-4.46	1.22	1.4621	0.0133	0.3542	0.0008	0.1299	0.0009
57623.477128	-6.16	1.48	1.4835	0.0134	0.3562	0.0010	0.1328	0.0010
57624.455987	-6.23	1.14	1.3930	0.0123	0.3510	0.0009	0.1299	0.0009
57625.548799	-6.86	1.22	1.4067	0.0107	0.3501	0.0008	0.1309	0.0008
57626.554737	-8.50	1.76	1.3159	0.0151	0.3482	0.0009	0.1280	0.0011
57627.535108	-5.02	1.61	1.2625	0.0159	0.3474	0.0011	0.1282	0.0012
57629.549641	-5.18	1.44	1.3152	0.0133	0.3471	0.0010	0.1248	0.0010
57630.536443	-7.73	1.54	1.1276	0.0156	0.3402	0.0011	0.1245	0.0012
57632.535169	-2.18	1.63	1.2713	0.0142	0.3436	0.0009	0.1269	0.0010
57635.392487	-0.29	1.19	1.3157	0.0109	0.3477	0.0008	0.1270	0.0008
57636.370440	-1.18	0.99	1.3496	0.0098	0.3481	0.0007	0.1302	0.0008
57637.516115	1.77	1.12	1.3111	0.0108	0.3475	0.0009	0.1298	0.0009
57638.545648	-2.87	1.45	1.3831	0.0135	0.3467	0.0009	0.1286	0.0010
57640.538743	1.73	0.86	1.3627	0.0105	0.3503	0.0006	0.1242	0.0007
57641.534605	3.05	1.03	1.3165	0.0122	0.3449	0.0008	0.1266	0.0009
57643.537577	2.60	1.06	1.4228	0.0138	0.3515	0.0009	0.1305	0.0010
57645.534503	-0.16	1.31	1.3778	0.0178	0.3520	0.0011	0.1279	0.0012
57646.524307	-1.35	1.02	1.4791	0.0116	0.3541	0.0007	0.1280	0.0008
57653.553135	1.14	1.43	1.6433	0.0218	0.3674	0.0011	0.1346	0.0013
57654.555535	1.42	1.63	1.6412	0.0215	0.3653	0.0010	0.1348	0.0012
57679.395908	3.04	1.16	1.4323	0.0128	0.3539	0.0007	0.1272	0.0009
57680.409564	2.54	1.20	1.3705	0.0118	0.3533	0.0010	0.1297	0.0009
57681.457267	-0.04	1.24	1.3597	0.0138	0.3547	0.0013	0.1346	0.0012
57683.438943	-1.91	1.36	1.4271	0.0142	0.3532	0.0009	0.1293	0.0010
57701.397060	-7.45	2.52	1.5908	0.0695	0.3524	0.0019	0.1311	0.0029
57702.391756	-10.58	2.53	1.2207	0.0327	0.3521	0.0015	0.1285	0.0020
57721.324810	-4.88	1.91	1.3428	0.0300	0.3470	0.0015	0.1299	0.0018
57859.730190	-2.26	2.28	1.1723	0.0352	0.3477	0.0016	0.1290	0.0020
57861.737737	1.98	1.35	1.3144	0.0160	0.3443	0.0009	0.1288	0.0011
57865.717589	1.83	1.90	1.6984	0.0333	0.3519	0.0014	0.1330	0.0018
57878.687660	5.46	1.24	1.4959	0.0184	0.3537	0.0009	0.1304	0.0012
57880.690696	2.55	1.35	1.5076	0.0146	0.3580	0.0009	0.1329	0.0010
57881.708813	1.11	1.21	1.4962	0.0229	0.3652	0.0012	0.1337	0.0014
57890.711349	0.05	2.10	1.4537	0.0291	0.3562	0.0015	0.1368	0.0018
57894.704442	1.82	1.19	1.4400	0.0122	0.3523	0.0008	0.1351	0.0009
57896.703867	4.42	1.54	1.4497	0.0155	0.3520	0.0009	0.1324	0.0011
57897.719003	2.20	1.31	1.4550	0.0157	0.3497	0.0009	0.1314	0.0011
57898.725167	0.41	0.83	1.4378	0.0104	0.3495	0.0007	0.1322	0.0008
57916.711750	5.64	1.14	1.3962	0.0139	0.3599	0.0011	0.1358	0.0011

Table A.1. Continued.

BJD - 2400000 (d)	RV (ms ⁻¹)	Δ RV (ms ⁻¹)	S-index	Δ (S-index)	H α -index	Δ (H α -index)	Na I-index	Δ (Na I-index)
57928.702352	6.03	4.73	1.1069	0.0671	0.3393	0.0017	0.1242	0.0035
57930.649599	10.56	2.14	1.2831	0.0230	0.3440	0.0009	0.1242	0.0014
57932.666903	1.58	1.22	1.2986	0.0130	0.3400	0.0008	0.1281	0.0009
57933.705004	0.59	1.26	1.3840	0.0144	0.3509	0.0009	0.1318	0.0010
57934.663692	1.63	2.51	1.2205	0.0352	0.3404	0.0015	0.1291	0.0021
57935.678133	0.74	2.21	1.2430	0.0230	0.3499	0.0012	0.1289	0.0015
57944.717102	-4.60	1.36	1.2721	0.0128	0.3418	0.0007	0.1253	0.0009
57952.634290	7.74	1.54	1.3957	0.0164	0.3541	0.0009	0.1327	0.0011
57953.620628	8.78	1.11	1.4560	0.0109	0.3577	0.0007	0.1314	0.0008
57969.481739	-1.55	1.42	1.2825	0.0184	0.3432	0.0011	0.1287	0.0013
57972.527474	2.69	1.68	1.1616	0.0146	0.3417	0.0010	0.1271	0.0011
57974.579433	-3.44	1.68	1.5073	0.0181	0.3527	0.0010	0.1360	0.0012
57976.626596	-6.89	1.58	1.2432	0.0152	0.3437	0.0009	0.1259	0.0011
57977.476387	-7.18	1.68	1.2844	0.0178	0.3485	0.0012	0.1312	0.0013
57978.522875	-7.89	1.23	1.2845	0.0113	0.3427	0.0008	0.1275	0.0009
57979.533008	-5.14	1.37	1.2524	0.0150	0.3413	0.0011	0.1294	0.0012
57980.524437	-5.09	1.12	1.2436	0.0102	0.3434	0.0008	0.1260	0.0008
57981.531616	-4.30	1.26	1.3445	0.0130	0.3425	0.0008	0.1273	0.0009
57984.545703	-1.78	1.58	1.2999	0.0187	0.3441	0.0011	0.1240	0.0013
57991.578297	16.01	3.53	1.6449	0.0664	0.3484	0.0014	0.1182	0.0026
57993.584859	8.69	1.61	1.4253	0.0183	0.3506	0.0008	0.1259	0.0011
57995.488618	3.24	1.78	1.4359	0.0197	0.3534	0.0010	0.1285	0.0013
57997.489417	-1.74	1.44	1.3938	0.0202	0.3547	0.0011	0.1302	0.0013
58000.496416	2.97	1.59	1.3261	0.0159	0.3527	0.0011	0.1291	0.0012
58005.520203	-2.82	1.23	1.4496	0.0134	0.3561	0.0008	0.1278	0.0009
58006.527222	-2.75	1.54	1.3786	0.0166	0.3547	0.0009	0.1222	0.0011
58007.519612	0.12	1.57	1.3121	0.0161	0.3507	0.0009	0.1281	0.0011
58008.508170	-1.55	1.33	1.3316	0.0121	0.3521	0.0008	0.1276	0.0009
58009.518323	-1.39	3.10	1.3530	0.0494	0.3518	0.0018	0.1327	0.0025
58010.527329	1.69	1.58	1.3843	0.0161	0.3481	0.0009	0.1264	0.0011
58011.410126	-1.12	1.16	1.3190	0.0145	0.3504	0.0010	0.1330	0.0011
58024.541278	0.95	1.54	1.3241	0.0185	0.3459	0.0009	0.1257	0.0011
58025.371544	1.20	1.39	1.2873	0.0106	0.3445	0.0008	0.1268	0.0008
58031.495137	0.25	1.69	1.4461	0.0153	0.3483	0.0009	0.1335	0.0011
58037.441370	4.77	1.85	1.5957	0.0214	0.3530	0.0010	0.1317	0.0013
58333.524276	7.28	1.61	1.3096	0.0121	0.3452	0.0009	0.1282	0.0010
58334.519679	5.84	1.43	1.3670	0.0137	0.3413	0.0010	0.1314	0.0011
58335.503783	8.15	4.77	2.0728	0.1667	0.3382	0.0038	0.1319	0.0075
58443.358465	3.62	1.18	1.2693	0.0118	0.3384	0.0008	0.1258	0.0009
58446.338876	-4.56	2.05	1.1359	0.0278	0.3387	0.0012	0.1284	0.0017
58974.692775	2.03	1.56	1.2699	0.0143	0.3461	0.0009	0.1262	0.0011
58976.693276	5.43	1.91	1.2408	0.0166	0.3468	0.0010	0.1265	0.0012
58985.653439	1.51	1.99	1.3204	0.0154	0.3511	0.0009	0.1282	0.0011
59007.691145	-0.18	1.32	1.1632	0.0090	0.3409	0.0008	0.1277	0.0008
59050.687681	-4.26	1.52	1.2192	0.0120	0.3381	0.0009	0.1209	0.0009
59051.675891	-2.99	1.51	1.2805	0.0135	0.3445	0.0007	0.1212	0.0009
59068.490382	9.43	1.47	1.5259	0.0148	0.3536	0.0007	0.1263	0.0010
59069.572791	-0.57	1.31	1.5124	0.0113	0.3565	0.0007	0.1306	0.0008
59070.632248	-1.41	1.26	1.5447	0.0148	0.3515	0.0008	0.1308	0.0010
59071.656784	-1.96	1.69	1.4222	0.0196	0.3489	0.0010	0.1301	0.0012
59111.440202	0.82	1.62	1.3842	0.0147	0.3475	0.0012	0.1292	0.0012
59125.467731	3.12	1.41	1.3467	0.0187	0.3399	0.0009	0.1223	0.0012
59126.368868	-1.78	1.46	1.2907	0.0120	0.3401	0.0007	0.1220	0.0009
59130.372594	-8.46	2.44	1.3283	0.0269	0.3395	0.0012	0.1219	0.0016